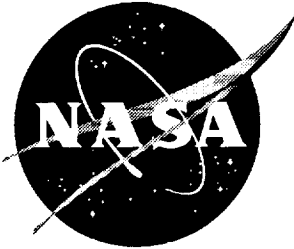


NASA/TP-1999-209543



Unstructured Grid Euler Method Assessment for Longitudinal and Lateral/ Directional Aerodynamic Performance Analysis of the HSR Technology Concept Airplane at Supersonic Cruise Speed

Farhad Ghaffari
Langley Research Center, Hampton, Virginia

December 1999

The NASA STI Program Office . . . in Profile

Since its founding, NASA has been dedicated to the advancement of aeronautics and space science. The NASA Scientific and Technical Information (STI) Program Office plays a key part in helping NASA maintain this important role.

The NASA STI Program Office is operated by Langley Research Center, the lead center for NASA's scientific and technical information. The NASA STI Program Office provides access to the NASA STI Database, the largest collection of aeronautical and space science STI in the world. The Program Office is also NASA's institutional mechanism for disseminating the results of its research and development activities. These results are published by NASA in the NASA STI Report Series, which includes the following report types:

- **TECHNICAL PUBLICATION.** Reports of completed research or a major significant phase of research that present the results of NASA programs and include extensive data or theoretical analysis. Includes compilations of significant scientific and technical data and information deemed to be of continuing reference value. NASA counterpart of peer-reviewed formal professional papers, but having less stringent limitations on manuscript length and extent of graphic presentations.
- **TECHNICAL MEMORANDUM.** Scientific and technical findings that are preliminary or of specialized interest, e.g., quick release reports, working papers, and bibliographies that contain minimal annotation. Does not contain extensive analysis.
- **CONTRACTOR REPORT.** Scientific and technical findings by NASA-sponsored contractors and grantees.

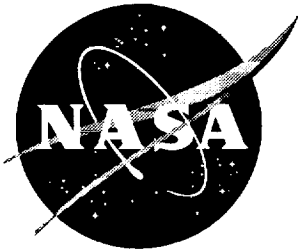
- **CONFERENCE PUBLICATION.** Collected papers from scientific and technical conferences, symposia, seminars, or other meetings sponsored or co-sponsored by NASA.
- **SPECIAL PUBLICATION.** Scientific, technical, or historical information from NASA programs, projects, and missions, often concerned with subjects having substantial public interest.
- **TECHNICAL TRANSLATION.** English-language translations of foreign scientific and technical material pertinent to NASA's mission.

Specialized services that complement the STI Program Office's diverse offerings include creating custom thesauri, building customized databases, organizing and publishing research results . . . even providing videos.

For more information about the NASA STI Program Office, see the following:

- Access the NASA STI Program Home Page at <http://www.sti.nasa.gov>
- Email your question via the Internet to help@sti.nasa.gov
- Fax your question to the NASA STI Help Desk at (301) 621-0134
- Telephone the NASA STI Help Desk at (301) 621-0390
- Write to:
NASA STI Help Desk
NASA Center for Aerospace Information
7121 Standard Drive
Hanover, MD 21076-1320

NASA/TP-1999-209543



Unstructured Grid Euler Method Assessment for Longitudinal and Lateral/ Directional Aerodynamic Performance Analysis of the HSR Technology Concept Airplane at Supersonic Cruise Speed

Farhad Ghaffari
Langley Research Center, Hampton, Virginia

National Aeronautics and
Space Administration

Langley Research Center
Hampton, Virginia 23681-2199

December 1999

Available from:

NASA Center for Aerospace Information (CASI)
7121 Standard Drive
Hanover, MD 21076-1320
(301) 621-0390

National Technical Information Service (NTIS)
5285 Port Royal Road
Springfield, VA 22161-2171
(703) 605-6000

Unstructured Grid Euler Method Assessment for Longitudinal and Lateral/Directional Aerodynamic Performance Analysis of the HSR Technology Concept Airplane at Supersonic Cruise Speed

Farhad Ghaffari
NASA Langley Research Center, Hampton, VA

Summary

Unstructured grid Euler computations, performed at supersonic cruise speed, are presented for a High Speed Civil Transport (HSCT) configuration, designated as the Technology Concept Airplane (TCA) within the High Speed Research (HSR) Program. The numerical results are obtained for the complete TCA cruise configuration which includes the wing, fuselage, empennage, diverters, and flow through nacelles at $M_\infty = 2.4$ for a range of angles-of-attack and sideslip. Although all the present computations are performed for the complete TCA configuration, appropriate assumptions derived from the fundamental supersonic aerodynamic principles have been made to extract aerodynamic predictions to complement the experimental data obtained from a 1.675%-scaled truncated (aft fuselage/empennage components removed) TCA model. The validity of the computational results, derived from the latter assumptions, are thoroughly addressed and discussed in detail. The computed surface and off-surface flow characteristics are analyzed and the pressure coefficient contours on the wing lower surface are shown to correlate reasonably well with the available pressure sensitive paint results, particularly, for the complex flow structures around the nacelles. The predicted longitudinal and lateral/directional performance characteristics for the truncated TCA configuration are shown to correlate very well with the corresponding wind-tunnel data across the examined range of angles-of-attack and sideslip. The complementary computational results for the longitudinal and lateral/directional performance characteristics for the complete TCA configuration are also presented along with the aerodynamic effects due to empennage components. Results are also presented to assess the computational method performance, solution sensitivity to grid refinement, and solution convergence characteristics.

SYMBOLS

b	reference span, 1575.1 inches
\bar{c}	reference chord, 1139.4 inches
C_D	drag coefficient, Drag/ $(q_\infty S_{ref})$
$C_{D,f}$	skin friction coefficient at $C_L = 0$
$C_{D,l}$	drag-due-to-lift coefficient at $C_L = 0$
$C_{D,o}$	drag coefficient at $C_L = 0$
$C_{D,p}$	pressure drag coefficient, pressure/ $(q_\infty S_{ref})$
$C_{D,w}$	wave drag coefficient at $C_L = 0$
C_L	lift coefficient, Lift/ $(q_\infty S_{ref})$
C_Y	side-force coefficient, (side-force)/ $(q_\infty S_{ref})$
C_l	rolling moment coefficient, Rolling moment/ $(q_\infty S_{ref} b)$
C_m	pitching moment coefficient, Pitching moment/ $(q_\infty S_{ref} \bar{c})$
C_n	Yawing moment coefficient, Yawing moment/ $(q_\infty S_{ref} b)$
C_p	pressure coefficient, $(p - p_\infty)/q_\infty$
M_∞	freestream Mach number
p	static pressure
p_∞	freestream static pressure
q_∞	freestream dynamic pressure
R_{ft}	Reynolds number per foot
S_{ref}	reference area, 1224112 sq. inches
x/c	fraction of wing local chord

$y(b/2)$	fraction of configuration semispan
α	angle of attack, degrees
β	sideslip angle, measured positive nose left, degrees
μ	semi-vertex Mach cone angle, degrees

Abbreviations

<i>FDS</i>	Flux Difference Splitting
<i>HSCT</i>	High Speed Civil Transport
<i>HSR</i>	High Speed Research
<i>IGES</i>	Initial Graphics Exchange Specification
<i>LaRC</i>	Langley Research Center
<i>NAS</i>	Numerical Aerodynamic Simulation
<i>PSP</i>	Pressure Sensitive Paint
<i>SST</i>	supersonic transport
<i>TCA</i>	Technology Concept Airplane
<i>UPWT</i>	Unitary Plan Wind-Tunnel
<i>NASA</i>	National Aeronautics and Space Administration

Introduction

Scientists and engineers from both NASA and U.S. aircraft industry are working towards developing the necessary technology for the design of the next generation supersonic transport airplane. This effort is being planned and coordinated through NASA's High-Speed Research (HSR) Program which is being managed at the NASA Langley Research Center (LaRC). The HSR program, initiated in late 1980's, rejuvenated an earlier U.S. supersonic transport (SST) program which was canceled in 1971 due to environmental and performance issues (Ref. 1). As a result, the issues that caused the cancellation of the SST program became the major technical challenges of the new HSR program. These technical challenges, recognized as level-I milestones within HSR program, are broken down into three categories: technology integration and environmental impact, propulsion technology, and airframe technology. The emerging vehicle design from the ongoing research, known as the Technology Concept Airplane (TCA), is a jet-fueled, four engine, cranked delta wing configuration. The TCA configuration is envisioned to cruise at Mach 2.4, carrying 300 passengers, over a 5,000 nautical miles.

The present effort is conducted to support the HSR level-II milestone (i.e., aerodynamic performance) under airframe technology. The objective of this study is to evaluate an existing unstructured grid Euler method, developed at NASA LaRC, for predicting the aerodynamic performance of the TCA configuration at the designed supersonic cruise speed. The ability of this particular method, known as USM3D (Ref. 2), has already been successfully demonstrated for predicting the transonic aerodynamic performance of a similar class of vehicle (i.e., Reference H configuration) for designed cruise (control surfaces appropriately deflected) and off-designed cruise configurations (Ref. 3). Similarly, this method is also being evaluated to explore the potential application for predicting aerodynamic characteristics of the TCA configuration at subsonic high-lift conditions. The documented results from these applications are providing valuable data for assessing the aerodynamic performance prediction capability of the method for the HSCT class of vehicle across the relevant speed regimes. Once calibrated, the method can then be used, with confidence, in the early design and aerodynamic analysis of the vehicle within the HSR program.

The primary objective of the present effort is to evaluate the USM3D method for predicting longitudinal and lateral/directional aerodynamic performance characteristics of the TCA configuration at the design supersonic cruise Mach number of 2.4. Due to the inviscid nature of the present analysis, the evaluation emphasis is placed on the method's ability to predict the aggregate forces and moments acting on the configuration accurately and not necessarily the detail flow physics. In spite of this fact, some representative

samples of the predicted flow structures are presented. Complementary to existing wind-tunnel data obtained in the NASA LaRC Unitary Plan Wind Tunnel (UPWT), a computational matrix is developed for the present numerical analysis. This matrix includes flow conditions across a wide range of α at $\beta = 0^\circ$ for the longitudinal and a wide range of β at $\alpha = 0^\circ$ for the lateral/directional analysis.

Experimental Data

The experimental test was conducted in the LaRC UPWT using a 1.675%-scale model of the truncated (aft-fuselage/empennage removed) TCA model. Figure 1 shows the sting-mounted truncated TCA model as installed in the UPWT from two different vantage points. In addition to the wing and the truncated fuselage (empennage also removed), this model consists of flow through nacelles and diverters. The primary objective of the test was to acquire the supersonic longitudinal and lateral/directional stability characteristics for evaluating the configuration aerodynamic performance at cruise ($M_\infty = 2.4$) as well as limited off-cruise speed conditions. As a result, the test matrix included only the supersonic cruise configuration, i.e., no deflection angles for the control surfaces such as the leading-edge and trailing-edge flaps. Furthermore, the experimental data for sideslip angles were only obtained at zero degree angle-of-attack. The typical Reynolds number for the test was about 4 million per-foot. In addition to the force and moment measurements, very limited Pressure Sensitive Paint (PSP) and surface pressure data are obtained for selected flow conditions. The available pressure data are used in the present analysis to gauge the prediction accuracy level and to demonstrate the ability and/or inability of the Euler method in predicting the pertinent flow physics associated with such a vehicle class and conditions.

Computational Approach and Attributes

Numerical Modeling Approach

In the present computational effort, the complete TCA configuration is modeled including the aft-fuselage and empennage components. Solid surface representation of the numerical TCA model is shown in figure 2 from two different perspective views. Although the experimental data have been obtained with the truncated TCA model, provisions have been made for extracting complementary aerodynamic characteristics from the present computational analysis of the complete TCA model. This provision is based on an assumption, derived from the fundamental supersonic aerodynamic principle, that simply states that any flow disturbance caused by a source in a supersonic medium does not propagate beyond its Mach cone. Based on this principle, it is assumed in the present numerical approach that any flow disturbance caused by the presence of the empennage is confined to a Mach cone originated from the longitudinal station where the empennage is truncated from the wind-tunnel model. The latter Mach cone and the corresponding semi-vertex Mach angle (μ) is defined as:

$$\mu = \sin^{-1}(1/M_\infty)$$

The schematic diagram shown in figure 3 illustrates approximately the corresponding Mach cone with semi-vertex Mach angle of $\mu = \sin^{-1}(1/M_\infty) = \sin^{-1}(1/2.4) = 24.6^\circ$ over the complete TCA planform for the present supersonic cruise Mach number (i.e., 2.4). The computational results for the truncated TCA model, extracted from the complete TCA numerical simulations, have been validated and are discussed in the next section.

There are two clear advantages associated with modeling the complete TCA configuration in the present investigation. The obvious advantage is the efficient utilization of the computer resources, i.e., one computational solution provides results for both the complete TCA model and the truncated TCA model. The second advantage is that the computational results for the complete TCA model provide valuable aerodynamic performance predictions for which no experimental data exist presently within the HSR program. Although the latter aerodynamic predictions for the complete TCA model are not calibrated directly against experimental data, but a subset of which has been calibrated for the truncated TCA model.

Computational Matrix

The UPWT experimental data are analyzed prior to the development of the computational matrix to identify appropriate range of angle-of-attack and sideslip angle for the supersonic cruise Mach number of 2.4. Subsequently, this analysis led to the selection of an α -range (i.e., $-3.5^\circ, 0^\circ, 3.5^\circ, 6^\circ$, and 8°) at $\beta = 0^\circ$ for the longitudinal and a β -range (i.e., $1.5^\circ, 3^\circ, 4.5^\circ$, and 6°) at $\alpha = 0^\circ$ for the lateral/directional aerodynamic performance analysis.

Flow Solver

All the numerical results presented in this report are computed using the flow solver USM3D (Ref. 2) which is developed at NASA LaRC. The time dependent, three dimensional Euler equations are solved by the method to simulate the inviscid flow within a computational domain discretized by tetrahedral-mesh elements. USM3D is based on cell centered, finite volume approach, and uses upwind-biased Flux-Difference-Splitting (FDS) scheme (Ref. 4) for spatial discretization of the flow primitive variables. Flow solutions are advanced by the implicit time integration approach (Ref. 5) with convergence accelerated to steady state by local time stepping and implicit residual smoothing. All computations presented in this report are obtained with the second-order FDS scheme, *minmod* limiter and 3-stage subiterations for implicit Gauss-Seidel time stepping. Flow tangency boundary condition is used everywhere on the configuration solid surfaces except on the blunt base at the nacelles exhaust face where a solution defined transpiration boundary condition is invoked to simulate a trailing wake-like flow (Ref. 6). This blunt-base boundary condition has been shown to improve solution convergence for variety of applications, such as a blunt wing trailing-edge, where the inviscid flow assumption causes a flow singularity at the surface discontinuities such as a sharp corner.

Computational Grid Discretization & Attributes

The initial TCA geometry is defined parametrically in a format known as Initial Graphics Exchange Specification (IGES), Ref. 7. This geometry served as the database for all the subsequent grid generation processes. GridTool (Ref. 8) is primarily used to discretize the geometry into various surface patches which are then fed into VGRID (Ref. 9, 10) for generating the initial surface triangulation by the advancing front method. The initial surface triangles, also referred to as the initial advancing front, are then read back into the GridTool program for the projection onto the initial database defined in IGES format. The projection process of the initial front onto the initial database is required in order to preserve the proper surface curvature within the interior of a given patch. Near-field and close-up views of the surface triangles are shown in figure 4 from two different vantage points. Finally, the projected surface triangles and the defined farfield boundary patches are used by VGRID to generate the volume grid within the computational domain along with the corresponding grid and face connectivity files for the flow solver. The flow field grid generated for the present analysis effectively utilized the newly developed feature of VGRID allowing the stretching of the grids in any direction on the surface or in the field. The computational grid is generally stretched on the surface along all the leading edges of various components such as the wing, the empennage and the exterior corners of the nacelles. The grid stretching rate-factor is strategically chosen for various regions of the configuration to efficiently model the local geometrical features and/or the expected flow physics. The grid stretching rate-factor is varied anywhere between 1.05 to 1.3 for different regions and generally the higher rate-factor is applied to the field grid in the radial direction at a distance slightly away from the surface.

The farfield boundary faces of the computational domain, shaped as a rectangular parallelepiped, are located at about $10.5\bar{c}$ upstream, $14\bar{c}$ downstream, $3.5\bar{c}$ span-wise, and $9\bar{c}$ above and below the numerical model (see figure 5(a)). For reference, $\bar{c} \approx 1140$ inches and the origin of the reference coordinate system ($X=0$, $Y=0$, and $Z=0$) is defined to coincide with the nose apex and the overall configuration body-length is about 3,912 inches in full-scale dimension. For all the zero sideslip computations the flow, simulated only over one-half of the model, is assumed to be fully symmetrical about the configuration plane of symmetry. A nearfield view of the computational grids in the plane of symmetry is shown in figure 5(b). This baseline grid consisted of about 60,000 surface triangles (see figure 4) and about 670,000 tetrahedral cells in the

computational domain. Typical cell height next to the surface is about $0.016\bar{c}$ and about 8 to 10 tetrahedral edges are used to define the inboard wing round leading edge curvature which roughly extends back about 1% of the local chord. As will be discussed in the grid sensitivity analysis of the next section, this grid is shown to be adequate for proper resolution of the flow characteristics across the present computational matrix.

Longitudinal Aerodynamic Analysis

In this section the computational results are presented in three parts. The results are discussed, first, for the complete TCA numerical model, followed by the results for the truncated TCA flow simulation and validation, and finally, the correlations between the predictions and the measured data. The flow is assumed to be symmetrical about the configuration plane-of-symmetry for longitudinal aerodynamic analysis; thus, the computations have been performed only for one-half of model. In addition, the discussions pertaining to the typical on- and off-surface flow features will focus only on the results at $\alpha = 3.5^\circ$ (i.e., approximately the cruise angle-of-attack for the vehicle).

Complete TCA Flow Simulation

Computations are performed on the complete TCA configuration using the baseline grid for $\alpha = -3.5^\circ, 0^\circ, 3.5^\circ, 6^\circ$, and 8° at $M_\infty = 2.4$ and $\beta = 0^\circ$. In this section, numerical results are presented for typical flow features followed by integrated force and moment predictions for both the complete TCA and the truncated TCA configuration. For comparison purposes between various results, efforts are made to limit the contour levels and range, associated with the on- and off-surface flow characteristics (i.e., surface pressure coefficients and Mach number), the same throughout this report. In addition, the grid sensitivity effects on the solution along with the algorithm convergence and performance characteristics are also discussed.

Typical flow features - The surface pressure coefficient contours computed at the design supersonic cruise angle-of-attack of $\alpha = 3.5^\circ$ for the complete TCA configuration are shown in figure 6 for the upper and lower surface. Although the numerical solutions have been obtained with one-half of the TCA model, the results have been mirrored about the configuration plane-of-symmetry.

The computed lower-surface pressure coefficients (fig. 6(a)) can generally be characterized by the flow compression around the nose apex region, the inboard/outboard wing leading-edges and a complex shock wave structure around the engine nacelles. For the inboard wing, the footprint of this compressed flow (i.e., $(C_p)_{max} \approx 0.1$) is confined to a narrow band that runs parallel along the leading-edge, whereas, for the outboard wing, the corresponding footprint (i.e., $(C_p)_{max} \approx 0.15$) appears to be wider on the lower surface spreading downstream to about one-half of the local chord. The high pressure footprints around the engines are associated with the shock waves emanating from both the inboard and outboard leading edges of the nacelles inlet lips and diverters. The general character of these shock waves form a very complex structure in and around the engine nacelles and are re-examined later in conjunction with the PSP data correlation. The computed upper surface pressure coefficients (fig. 6(b)) reveal a fairly benign distribution over the forebody and a region of flow expansion that runs parallel to the inboard wing leading-edge which extends onto the wing outboard panel. This pressure distribution also indicates a slight flow expansion around the leading edge of the outboard wing along with a region of compression around the horizontal-tail leading-edge.

The off-surface flow-field characteristics are also examined using a variety of flow variables such as the total pressure coefficient, density, and Mach number, in an attempt to highlight the relevant features of the flow-field. It was subsequently determined that the Mach number contours consistently highlighted the most relevant flow-field information for the subject analysis. A typical result showing the Mach contours in the plane-of-symmetry along with the surface pressure coefficient contours is presented in figure 7, from two different angles. The surface pressure coefficients are plotted over the same range as the previous figure and the Mach numbers are contoured over a compressed range of 2.3 to 2.4. This limited range of Mach number is found to be sufficient to accentuate the main flow features in the majority of the flow field. Over

this contour range, the Mach numbers exceeding 2.4 (i.e., free stream cruise Mach) are shown white, while, Mach numbers below 2.3 are shown in black indicating a slower moving flow relative to the free stream. The Mach contours clearly show various Mach lines in the plane-of-symmetry, caused by either the presence of a local geometry, or the footprints of reflected flows caused by other geometrical components such as the nacelles and diverters. This latter footprint is clearly evident as the off-surface extension of the shock wave emanates from the leading edge of the inboard nacelle intersecting the plane-of-symmetry.

The computed results also show complex flow characteristics on the interior and exterior surfaces of the nacelles. To illustrate the complexity of the nacelles interior flow, a close-up view of the computed surface pressure coefficients (shown earlier in figure 6(a)) is presented in figure 8(a). The latter figure is repeated in figure 8(b), but it includes the Mach number variations in two stream wise planes (parallel to the configuration plane-of-symmetry) that roughly cut through the mid-outboard nacelle (i.e., $y=370$ inches) and the mid-inboard nacelle (i.e., $y=206$ inches). For consistency, the Mach variations in these planes are contoured over the same range as figure 7. The Mach variations in the outboard plane clearly indicate a region of flow compression around the wing leading-edge followed by another region of expansion and compression before reaching the nacelle inlet. The outboard nacelle interior flow structure can be characterized by a series of shock waves that bounce back and forth, creating regions of flow expansion and compression on the interior surfaces of the nacelle, as evident from the surface pressure distribution. Similar Mach variations can also be seen in the interior flow structures of the inboard nacelle.

Complementary to figures 7 and 8(b), figure 9 shows the similar Mach variations but for several longitudinal cross-flow planes. The figures show the results on the pitched up vehicle viewed from the front. Both the Mach numbers and surface pressure coefficients are contoured over the same range as the previous figures. Figures 9(a)-(h) show the surface C_p along with the Mach variations in six longitudinal cross-flow planes at $X=1200, 2300, 2570$ (includes a close up), 2750 (includes a close up), 3200 , and 4000 inches, respectively.

The Mach number distribution in the first two cross-flow planes (figures 9(a)-(b)) clearly show the circular pattern indicative of the cuts through the Mach cone over the forebody and mid-wing region. Also, note that the Mach contours indicate a region of flow compression over the wing lower surface (i.e., figure 9(b)), covering about one-half of the outboard local-span, leading to a flow expansion around the leading edges to the upper surface. The Mach variations are shown in figure 9(c) for a longitudinal cross-flow plane just aft of the nacelle inlet-faces and the wing leading-edge break point. A close up view of the flow features around the nacelles, from the latter figure, is shown in figure 9(d). The Mach number distribution indicates the presence of a flow compression-band around the exterior surfaces of the outboard nacelles that develops into a larger region as it extends outboard toward the wing leading-edges. Also note the Mach expansion ($M_\infty > 2.4$ represented by white region) between the two inboard nacelles. The primary flow feature associated with the Mach number variations in cross-flow planes shown in figures 9(e)-(f) is the expanded compression region around the outboard nacelles along with the off-surface extension of the shock waves (i.e., inboard leg close to the plane-of-symmetry) emanating from the inboard nacelle diverter. The results clearly indicate that the latter standing shock-waves bend outboard and impinge on the exterior side of the inboard nacelle. Finally, the Mach number distributions are shown in two cross-flow planes, one just ahead of the empennage (figure 9(g)) and the other located just behind the configuration (figure 9(h)). The Mach variations in the latter two cross-flow planes illustrate the trailing wake structures associated with various regions of flow expansion and compression over the configuration.

Force and moment predictions - The computed longitudinal aerodynamic characteristics are presented in figure 10 for both the complete as well as the truncated TCA configuration at supersonic cruise Mach number of 2.4. Note that, as discussed earlier, the same numerical solution developed for the complete TCA configuration, at a given angle of attack, is also used to compute the forces and moment for the truncated TCA configuration, by only integrating the surface pressures over appropriate geometrical components.

The results for computed lift coefficients clearly indicate minimal effects due to the additional empennage loads at $\alpha = 3.5^\circ$ (i.e., close to the vehicle design cruise angle-of-attack). However, as expected for

off-design angles-of-attack, the additional load from the presence of the empennage on C_L becomes more pronounced, i.e., increase in C_L for $\alpha > 3.5^\circ$ and decrease in C_L for $\alpha < 3.5^\circ$. Although the latter effects on C_L are relatively small, the corresponding impact on the pitching moment characteristic is considerable due to the long moment arm. The results indicate that the additional load from the presence of the empennage on the pitching moment characteristics to be insignificant at $\alpha = 3.5^\circ$, cause a pitch down for $\alpha > 3.5^\circ$ and a pitch up for $\alpha < 3.5^\circ$. Furthermore, the empennage load increments on the computed drag coefficient appear to be small over the examined range of flow conditions. Note that the latter computed inviscid drag coefficients have not been corrected to account for the skin friction.

Grid sensitivities and solution convergence/performance - All the computational results presented so far are obtained using the so called baseline grid with certain attributes which were discussed earlier. As part of the present investigation, an effort is also made to evaluate the effects of flow-field grid resolution on the numerical solutions presented above. As a result, a finer field grid is generated using the baseline surface triangles as well as the farfield boundary faces without any alteration. The final grid, referred to as the fine grid, consisted of about 1.3 million tetrahedra which is roughly twice as fine everywhere as the baseline grid. Identical procedures are used to advance the solutions with USM3D flow solver as those used for earlier solutions obtained with the baseline grid.

Euler computations are performed, using the fine grid, across the angle-of-attack range of the present investigation. The computed flow field solutions, based on the fine grid, are analyzed and correlated with those obtained with the baseline grid. Although not presented in this report, in general, all flow field analyses indicated no distinguishable differences between the results obtained with the baseline and the fine grid. The effects of flow field grid resolution on the integrated forces and moment are also analyzed. Figure 11 shows the computed longitudinal aerodynamic characteristics with both the baseline as well as the fine grid. The result for each solution is presented in two forms: for the truncated TCA and the complete TCA configuration. The results clearly indicate that the grid refinement induces minimal effects on the predicted longitudinal aerodynamic characteristics throughout the examined range of angle-of-attack for both the complete and truncated TCA configuration.

All the present computations are performed on the numerical aerodynamic simulation (NAS) Cray-C90 computer located at NASA Ames Research Center. On this machine, the algorithm required about $21\mu\text{sec}$ per iteration per cell and about 120 million words of memory for the longitudinal computations (i.e., one-half the model) using the baseline grid. The memory requirement is doubled for all the computations with finite sideslip angle. Figure 12 shows the convergence characteristics for all the longitudinal computations on the complete TCA configuration using the baseline and the fine grid. The solution convergence for all the longitudinal computations is nominally achieved with about 150 iterations where the total residuals are dropped by approximately 3 to 4 orders of magnitude and reduced oscillations in C_L and C_D to a negligible level. Computation for a typical solution is started from free-stream conditions with the Courant, Friedrichs, Lewy (CFL) number initially set to 20 which is subsequently ramped up linearly to a value of 40 over the first 100 cycles. Note that the spikes occurring in the residual curves after about 50-60 cycles are associated with the tolerance level (presently set at an order of magnitude drop in the total residuals) built into the algorithm to automatically switch from first order to second order FDS formulation.

Truncated TCA Flow Simulation and Validation

This section presents the results from the calibration effort conducted to primarily evaluate the validity of the numerical solutions for the truncated TCA configuration which have been extracted from the complete TCA model simulation. In particular, this calibration effort is designed to validate the basic assumption by demonstrating that the flow disturbance caused by the presence of the empennage in the complete TCA numerical flow simulation is indeed confined to the Mach cone originated from the truncated longitudinal-station. The approach taken is to numerically model the actual truncated TCA configuration, as tested in the LaRC UPWT including the sting geometry, and correlate the results with those extracted from the complete TCA configuration. For consistency, the same surface triangles as those used in the complete TCA model are

used to represent the actual truncated TCA configuration. Subsequently, an approximate representation of the wind-tunnel model sting geometry is incorporated into the truncated TCA numerical model by repeating the last fuselage cross-section (i.e., longitudinal station where the empennage is truncated) to the downstream farfield boundary. Similar grid strategy, as those used to construct the baseline grid for the complete TCA configuration, is employed to generate a consistent field grid in terms of general distribution and number of points. The surface triangles for the truncated TCA numerical model, including the sting representation, along with the grids in the plane-of-symmetry are shown in figure 13. The final grid for the truncated TCA numerical model comprised of about 45,000 surface triangles and approximately 650,000 tetrahedral mesh in the computational domain. Computations are performed, for the truncated TCA numerical model, across the angle-of-attack range selected for the longitudinal aerodynamic analysis in the present investigation. The computational results are discussed in the following two sections for typical flow features and the integrated forces and moment.

Typical flow features - The surface pressure contours, computed at the supersonic cruise angle-of-attack of 3.5° for the truncated TCA configuration, are shown in figure 14, from identical vantage points and over the same range as the results shown earlier in figure 6 for the complete TCA configuration. The solid surface model for the sting geometry representation is also included in these figures. The computed results on the truncated TCA model clearly indicate surface pressure contours that are very close, both in terms of general characteristics and the magnitudes in various regions, to the solutions obtained over the same components (i.e., truncated TCA) from the complete TCA numerical model. Furthermore, the Mach number variations in several longitudinal cross-flow planes located at $X=2570, 2750, 3200$, and 4000 inches along with the computed surface pressure contours are shown in figure 15. These Mach number variations in different cross-flow planes complement those shown earlier for the complete TCA numerical results at the same longitudinal stations (i.e., figures 9(c), (e)-(h)). The Mach number distributions for the first two cross flow planes (i.e., figure 15(a)-(b)), obtained from the truncated TCA numerical simulation, clearly indicate very similar characteristics to those presented earlier for the complete TCA configuration at the same longitudinal stations (i.e., figure 9(c)-(e)). However, the Mach number variations shown in the last two cross flow planes (i.e., figure 15(c)-(d)) indicate certain characteristics that are different from those computed for the complete TCA (figure 9(g)-(h)), particularly at the last plane. Note that, relative to the complete TCA model, the latter two cross flow planes are located just ahead and just aft of the empennage geometries which are not modeled for the truncated TCA configuration. As a results, the local geometry perturbations (i.e., the lack of empennage presence) are expected to cause some differences in the solutions for near field region with diminishing effects away from the configuration in the radial direction.

Force and moment predictions - The longitudinal aerodynamic characteristics computed for the truncated TCA numerical model are presented in figure 16 across the examined angle-of-attack range. The complementary results extracted (i.e., for only the truncated TCA components) from the full TCA numerical model are also included for comparison. It should be noted that the predicted drag coefficients presented in the latter figure have not been corrected to account for the skin friction contribution. The results clearly indicate that nearly identical longitudinal aerodynamic characteristics can indeed be predicted for the truncated TCA configuration by either modeling the actual geometry or by integrating the pressures over the appropriate geometrical components from the numerical solutions obtained for the full TCA configuration. As a result, the validity of the present approach in modeling the full TCA configuration, not only to obtain the aerodynamic predictions for the complete vehicle but also for the truncated TCA portion of the configuration (i.e., proper integration of pressures for geometrical components), is clearly demonstrated.

Euler Drag Correction and Data Correlations

$C_{D,f}$ determination - There are two aerodynamic phenomena contributing to the total drag force exerted on an airborne vehicle, the viscous (or the skin friction) component ($C_{D,f}$) and the pressure drag

(or the drag-due-to-lift or the vortex drag) component ($C_{D,p}$). In supersonic flow the pressure drag can be decomposed into the drag-due-to-lift ($C_{D,l}$) and the wave drag ($C_{D,w}$) components. Hence,

$$\begin{aligned} C_D &= C_{D,f} + C_{D,p} \\ C_D &= C_{D,f} + C_{D,l} + C_{D,w} \end{aligned}$$

The conventional approach is taken to correct the drag coefficients predicted by the present Euler analysis to account for the viscous component of the total drag coefficient. This correction is required primarily due to the inviscid nature of the present Euler analysis and the inherent ability of the corresponding equations to only predict the pressure components of the total drag. This conventional approach is based on determining the total drag coefficient at zero lift (i.e., $C_{D,o}$) using the experimental data for the drag polar curve. This approach is adopted and the $C_{D,o}$ is determined graphically, as shown in figure 17, to be 98.94 drag counts. Note that the cubic spline curve-fit is used to connect the experimental data points plotted over a small range to graphically determine the $C_{D,o}$ with reasonable accuracy. However, the determined $C_{D,o}$ is not only drag contribution due to viscosity but it also includes wave drag component (i.e., $C_{D,o} = C_{D,f} + C_{D,w}$). In an effort to isolate the wave drag component from the determined $C_{D,o}$, the baseline unstructured-grid developed earlier for the Euler analysis of the truncated TCA model is employed to compute the flow at $\alpha = 0.2^\circ$ which was found to correspond to the experimental zero-lift data (see figure 18). The latter computation was performed and the corresponding lift coefficient was predicted indeed very close to the expected value of zero, as shown in figure 19, and thus correlated well with the experimental data. Therefore, it is assumed that the pressure drag coefficient predicted by the Euler method is solely the wave drag component ($C_{D,w}$) with no contribution from drag-due-to-lift ($C_{D,l}$). The resulting wave drag coefficient is computed to be 31.27 counts. As a result, the skin friction contribution to the total drag for the truncated TCA configuration is found to be $98.94 - 31.27 = 67.67$ counts. This skin friction contribution, assumed to remain constant with α and β , is used to correct all the drag coefficient predictions in the present Euler analysis for the truncated as well as the full TCA configuration.

Force and moment - The computed longitudinal aerodynamic characteristics are presented in figure 20 for both the complete and the truncated TCA configuration, along with the experimental data obtained with the truncated TCA model at supersonic cruise Mach number of 2.4. Note that the latter numerical results are identical to those shown earlier in figure 10 except for the drag coefficients which now include the skin friction component. The correlation between the predictions of experimental data for the truncated TCA configuration indicate excellent agreement for the pitching moment, lift and drag coefficients across the examined angle-of-attack range. It should also be noted that the computed drag coefficients presented for the complete TCA configuration do not include the skin friction contribution for the empennage components.

Surface pressure - A limited amount of PSP data were also acquired on the truncated TCA model during the UPWT test. Typical PSP data obtained over the wing lower-surface of the TCA supersonic cruise configuration (i.e., no control surface deflection) at $\alpha = 3.5^\circ$ and $M_\infty = 2.4$ is presented in the right hand-side of figure 21. Complementary to the experimental PSP result, the surface pressure coefficients computed for the same configuration and flow conditions, by the present Euler method, is shown from the same vantage point on the left hand-side of figure 21. The latter computational result is actually extracted from the same numerical solution that was presented earlier in figure 6. The pressure range and the corresponding color map have been changed to match that of the PSP data. The results clearly show that the three main flow features highlighted by a region of fairly benign pressure distribution on the inboard wing ahead of the nacelles, flow compression under the wing outboard section, and the general character of the complex shock wave structures around the nacelles have been predicted reasonably well. It should also be noted that the diffusive structure of the shock waves around the nacelles in the PSP result is primarily attributed to viscous effects which are not modeled by the Euler formulation.

There were also limited surface pressures measured in several chordwise stations on the truncated TCA model during the UPWT test. The left hand-side of figure 21 shows the relative locations of three

chordwise stations (i.e., $y(b/2) = 0.199, 0.413, 0.680$) selected for the present analysis and correlations with the numerical results. The measured surface pressure coefficients, obtained at $\alpha = 3.5^\circ$, $M_\infty = 2.4$, and $R_{ft} = 4 \times 10^6$, for the selected chordwise stations are shown in figure 22 along with the corresponding numerical predictions. The results clearly indicate a very good correlation between the measured and the predicted pressures on the upper surface at all three stations. Similarly, the lower surface pressure distribution is predicted fairly well except in the vicinity of the nacelles where the shock wave location, highlighted by the sudden pressure increase (i.e., $y(b/2)=0.199, 0.413$), are predicted further aft than the experimental data indicate. The lack of a good agreement between the measured and computed pressures, for the shock wave locations, in the vicinity of the nacelles is also evident in figure 21 discussed in the previous paragraph.

Lateral and Directional Aerodynamic Analysis

The computational results for sideslip angles (i.e., $\beta = 1.5^\circ, 3^\circ, 4.5^\circ$, and 6°) at $\alpha = 0^\circ$ for the complete TCA configuration at supersonic cruise speed are presented in this section. The unstructured grid for the computations is generated for the complete TCA by mirroring the baseline grid, developed earlier for the longitudinal analysis, about the configuration plane-of-symmetry. The resulting grid consisted of about 1.3 million tetrahedra and about 120,000 surface triangles. A typical sideslip computation required about 240 million words of memory and the algorithm took about $50\mu\text{sec}$ per iteration per cell. Similar procedures are used to advance the solutions for the each sideslip angle as those used for earlier computations at zero sideslip. The solution convergence characteristics for all the sideslip computations are presented in figure 23. Similar to the zero-sideslip computations, a typical solution convergence is nominally achieved with 150 cycles where the total residuals are dropped by about 4 orders of magnitude and reduced oscillations in C_L and C_D to a negligible level. However, the computations at 6 degree sideslip angle required 250 cycles to approximately converge to the same level of orders of magnitude as those achieved for lower sideslip angles. Unlike the computations at lower sideslip angles, the latter solution took about 100 cycles to achieve an order of magnitude drop in the residuals before the algorithm switched from the first order FDS approximation to the second-order.

Typical Flow Features - The surface pressure coefficient contours computed at $\alpha = 0^\circ$, $\beta = 3^\circ$ and $M_\infty = 2.4$ for the complete TCA configuration are shown in figure 24. These surface pressure coefficients are plotted consistent with the results for longitudinal analysis shown in figure 6, over the same contour range for both the lower and upper surface. Note that, in addition to the sideslip angle, the angle of attack is also different between the computational results shown in figures 24 and 6.

The computed surface pressure coefficients clearly show the expected asymmetrical load distribution on both lower and upper surface. The lower surface pressure contours indicate a region of expansion ($C_p \approx -0.2$) that runs roughly parallel to the starboard leading-edge of the inboard-wing, whereas, the pressure contours around the port-side leading-edge of the inboard wing indicate a fairly benign attached flow condition. The upper surface pressure contours indicate a uniform distribution over the majority of wing with a narrow band of compression along the starboard leading-edge of the inboard wing which expands over onto the outboard section. In addition, the computed upper surface pressure contours over the horizontal tails also show a large region of compression on the starboard side.

Typical off-surface flow characteristic and the corresponding effects on the wing lower-surface computed at $M_\infty = 2.4$, $\alpha = 0^\circ$ and $\beta = 3^\circ$ for the complete TCA configuration are shown in figure 25. Consistent with the earlier results for longitudinal analysis (i.e., figures 9(e) and 9(g)), the computed Mach number variations in two typical cross-flow planes, located at longitudinal stations $X=2750$ and $X=3200$ inches, in conjunction with the wing surface pressure contours, are shown in figures 25(a) and 25(b). The flow asymmetry due to sideslip angle is clearly shown in the cross-flow Mach number variations, particularly in figure 25(a), with respect to the shock wave structures in the vicinity of the nacelles and around the wing leading-edges.

Force and Moment Predictions and Correlation With Data - The overall aerodynamic force characteristics computed for the complete TCA configuration across the examined range of sideslip angles at $\alpha = 0^\circ$ and $M_\infty = 2.4$ are presented in figure 26. The experimental data for the truncated TCA model along with complementary results extracted from the full TCA numerical simulation (i.e., with appropriate component integration to only account for the truncated TCA geometry) are also included in figure 26.

The predicted side-force coefficients for the truncated TCA configuration are in excellent agreement with the experimental data, both in terms of magnitude and trends, across the examined range of sideslip angles. In general, the side-force coefficients appear to vary in a fairly linear fashion with sideslip angle. The results also indicate that the presence of empennage primarily effects the slope of the C_Y vs. β curve, but not its linear characteristic. This change in slope can mainly be attributed to the asymmetrical load contribution cause by the vertical-tail presence.

The measured lift coefficients for the truncated TCA model along with the numerical estimates for the complete as well as the truncated TCA configurations are presented in figure 26. Note the small scales for the plot and the resulting variations in lift coefficients for the all configurations across the examined range of sideslip angles. The computed lift coefficients for the truncated TCA configuration correlate very well across the range of measured data. The presence of the empennage also appears to cause a nearly constant increase to the overall lift coefficient, though in the negative direction, for all the sideslip angles considered in the present study.

The computed and the measured drag coefficients for the truncated TCA configuration are shown in figure 26 along with the numerical drag predictions for the complete TCA model. The same skin friction coefficient determined earlier, in conjunction with the longitudinal aerodynamic analysis (i.e., 67.67 drag counts), is also used to correct the drag coefficients predicted at finite sideslip angles. The results clearly show an excellent comparison between the measured and predicted drag coefficients for the truncated TCA configuration across the examined range of sideslip angles. Similar to the lift characteristics discussed in the previous paragraph, the presence of the empennage also appears to cause a nearly constant increase in the overall drag coefficient for all the sideslip angles considered in the present study. It should also be noted that, similar to the longitudinal analysis discussed earlier, the computed drag coefficients presented for the complete TCA configuration do not include the skin friction contribution for the empennage components.

The computed and measured aerodynamic moment characteristics for the truncated TCA configuration are presented in figure 27 for the supersonic cruise Mach number of 2.4 at zero degree angle of attack. Complementary numerical predictions for the complete TCA configuration are also included in figure 27 for comparison. In general, there is an excellent correlation between the numerical predictions and the experimental data for the aerodynamic moment characteristics of the truncated TCA configurations across the examined range of sideslip angles. As expected, the aerodynamic moments predicted for the complete TCA configuration clearly indicate dramatically different characteristics than those of the truncated TCA model. These differences in the moment characteristics are primarily due to the empennage components. For example, the results indicate a sign reversal in the yawing and rolling moments which can primarily be attributed to the presence of the vertical and the horizontal tails, respectively. Furthermore, the pitch-up moment characteristics for the complete TCA configuration can mainly be attributed to the negative load contributions due to the empennage presence (i.e., see figure 27).

CONCLUDING REMARKS

Inviscid supersonic flow results and analyses are presented for a High Speed Civil Transport (HSCT) configuration, designated as the Technology Concept Airplane (TCA), within the High Speed Research (HSR) Program. The numerical results, based on an unstructured grid Euler method, are obtained for the complete TCA configuration over a range of angle-of-attack and sideslip angles at the designed supersonic cruise Mach number of 2.4. An efficient numerical modeling approach, based on an assumption derived from the fundamental supersonic aerodynamic principles, has been devised to extract aerodynamic predictions to complement the experimental data obtained from the truncated (aft fuselage/empennage components removed) TCA wind-tunnel model. The validity and the accuracy of the results obtained from the latter

numerical modeling approach are also addressed.

The predicted surface pressure coefficient contours are analyzed and the complex shock-wave structures on the wing lower-surface around the nacelles are found to correlate reasonably well with the available Pressure Sensitive Paint results obtained at $\alpha = 3.5^\circ$, $M_\infty = 2.4$, and $\beta = 0^\circ$. The numerical results for the off-surface and the nacelles internal flow structures are also presented and analyzed. Though plausible, no experimental data are available to assess the corresponding prediction accuracy levels. The predicted longitudinal and lateral/directional aerodynamic performance characteristics for the truncated TCA configuration are shown to correlate very well with existing experimental wind-tunnel data across the examined range of α and β at $M_\infty = 2.4$. The complementary computational results for the longitudinal and lateral/directional performance characteristics for the complete TCA configuration are also presented along with the aerodynamic effects due to empennage components. In addition, results are presented to assess the computational method performance, solution sensitivity to grid resolution, and solution convergence characteristics.

The numerical results clearly indicate that the present unstructured grid Euler method is a viable tool that can be used, with confidence, for the aerodynamic analysis of the HSCT class of vehicle in the early configuration design cycle. The present analysis also indicates that the method is robust and produces consistent solutions across the examined range of conditions without any convergence difficulties.

REFERENCES

1. Willhite, A. W. and Shaw, R. J.: HSCT Research Picks Up Speed. *Aerospace America*, August 1997, pp. 24-29.
2. Frink, N. T.: Upwind Scheme for Solving the Euler Equations on Unstructured Tetrahedral Meshes. *AIAA Journal*, Vol. 30, No. 1, 1992, pp. 70-77.
3. Ghaffari, F.: Unstructured Grid Euler Method Assessment for Longitudinal and Lateral/Directional Stability Analysis of the HSR Reference H Configuration at Transonic Speeds. NASA CDTM-10008, February 1997.
4. Roe, P. L.: Characteristic-Based Scheme for the Euler Equations. *Annual Review of Fluid Mechanics*, Volume 18, Milton van Dyke, J. V. Wehausen, and John L. Lumley, eds., Annual Reviews Inc., 1986, pp. 337-365.
5. Anderson, W. K.: Grid Generation and Flow Solution Method for Euler Equations on Unstructured Grids. NASA TM-4295, April 1992.
6. Frink, N. T.; Pirzadeh, S.; and Parikh, P.: An Unstructured-Grid Software System for Solving Complex Aerodynamic Problems. NASA-CP-3291, May 1995.
7. Smith, B. M.; Brauner, K. M.; Kennicott, P. R.; Liewald, M.; and Wellington, J.: Initial Graphics Exchange Specification (IGES), Version 2.0. NBSIR-82-2631-AF, Feb. 1983. (Available from NTIS as PB 83-137448.)
8. Abolhassani, J.: GRIDTOOL: A Surface Modeling and Grid Generation Tool. NASA-CP-3291, May 1995, pp. 821-832.
9. Pirzadeh, S.: Recent Progress in Unstructured Grid Generation. AIAA Paper No. 92-0445, January 1992.
10. Parikh, P.; Pirzadeh, S.; and Lohner, R.: A Package for 3-D Unstructured Grid Generation, Finite-Element Flow Solution and Flow Field Visualization. NASA CR-182090, Sept. 1990.

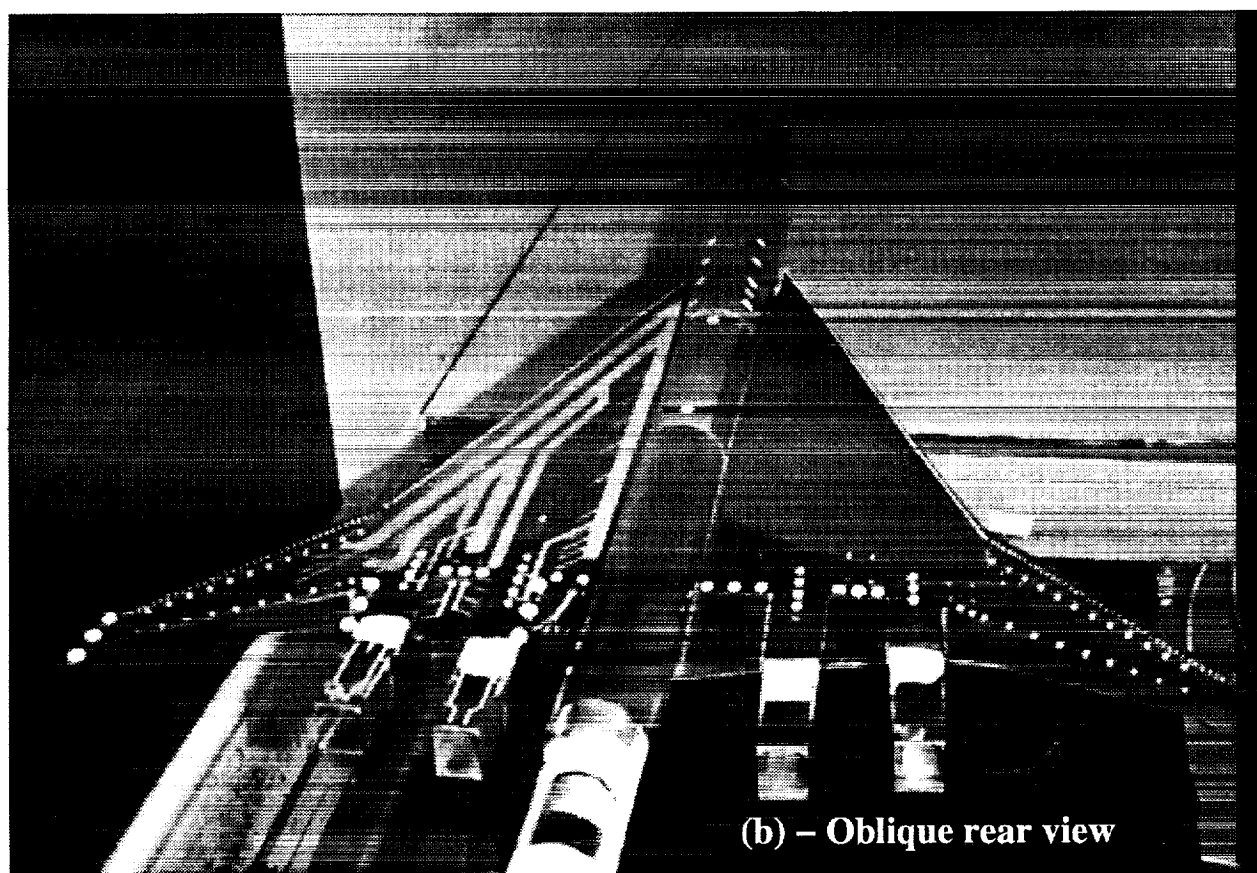
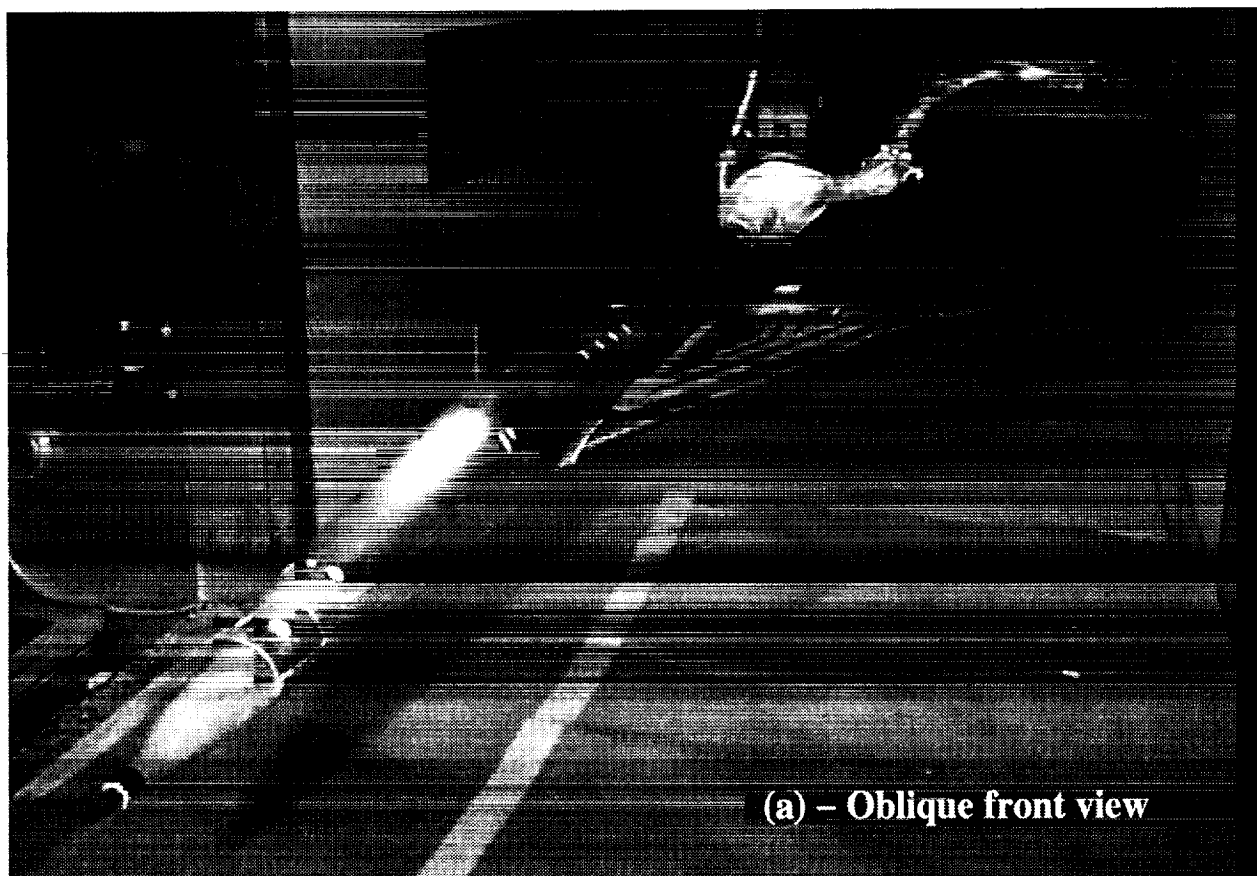
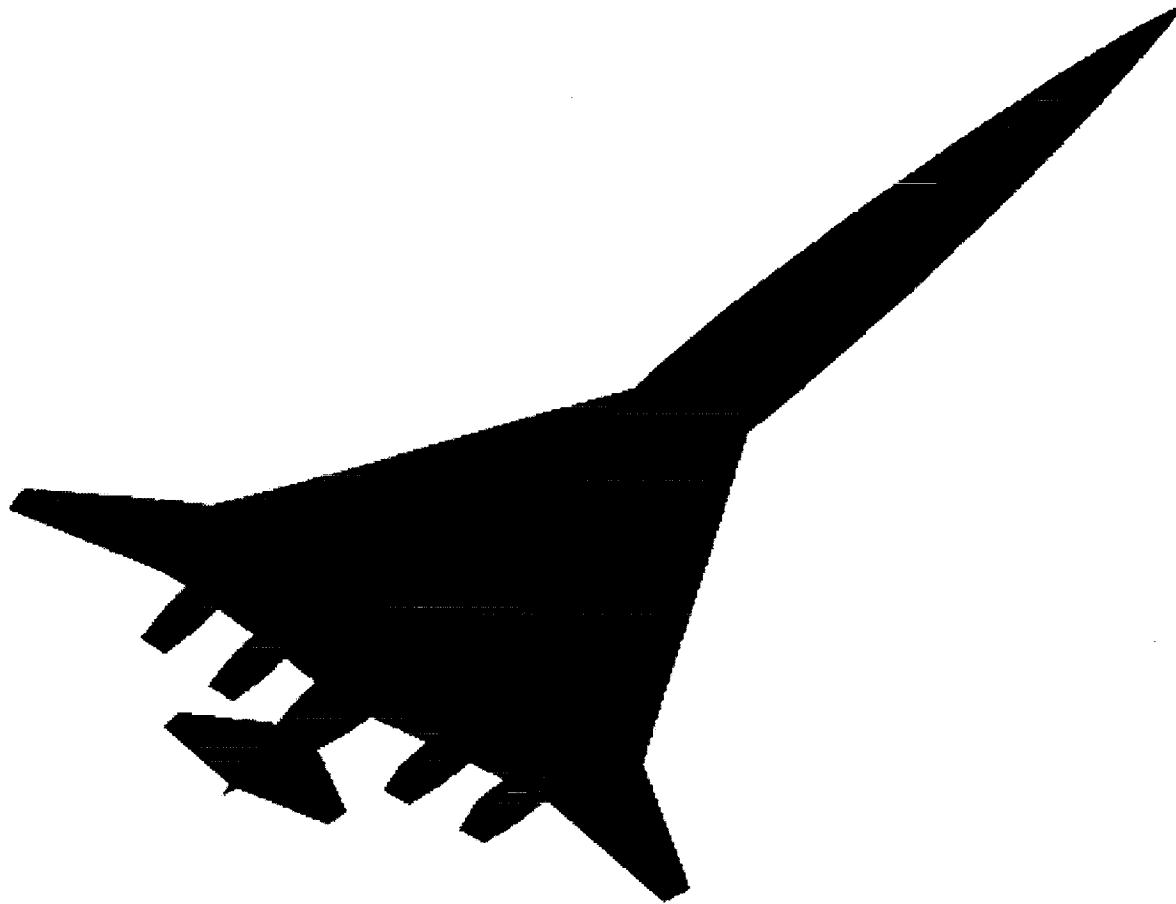
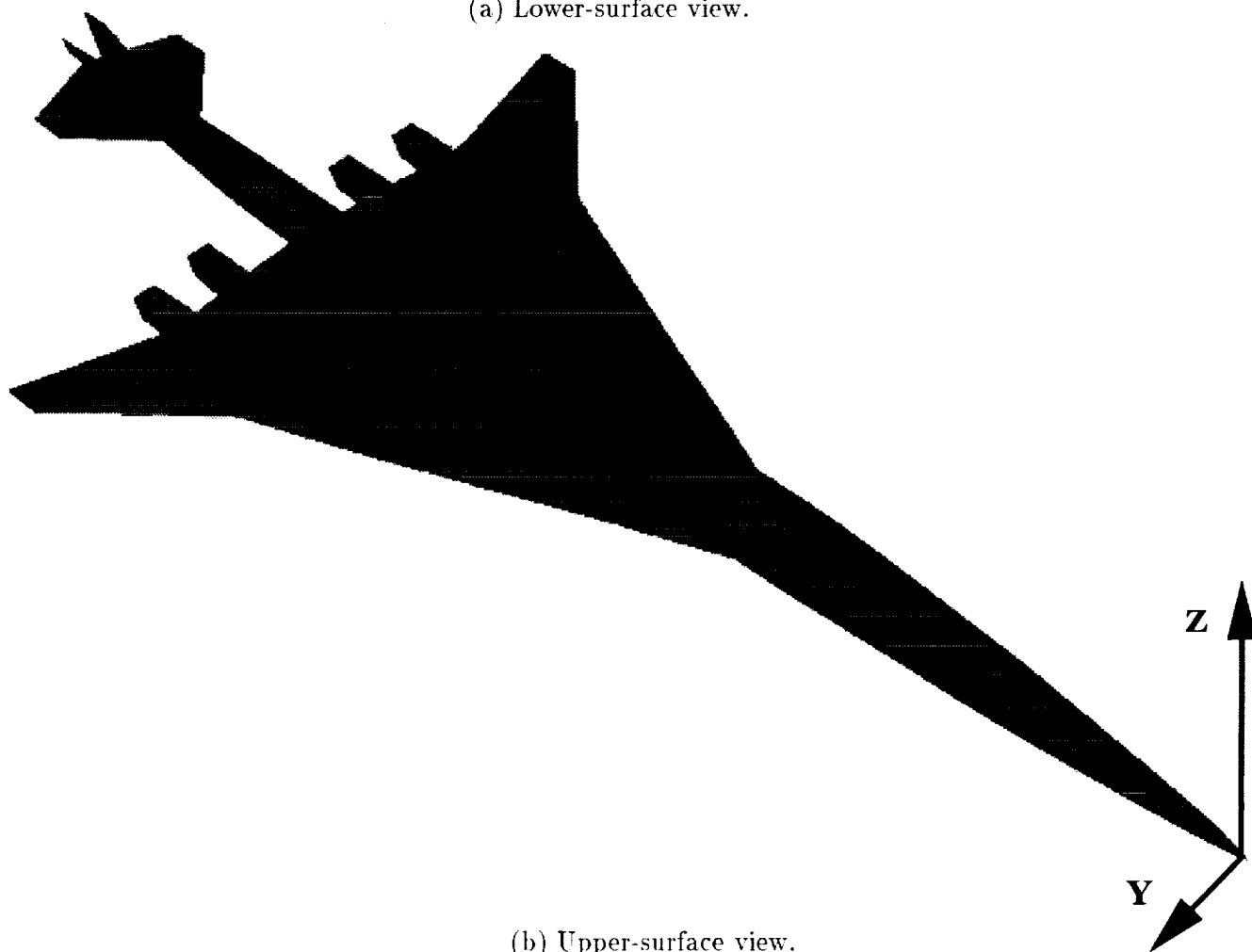


Figure 1. 1.675%-scale truncated TCA wind-tunnel model in LaRC UPWT.

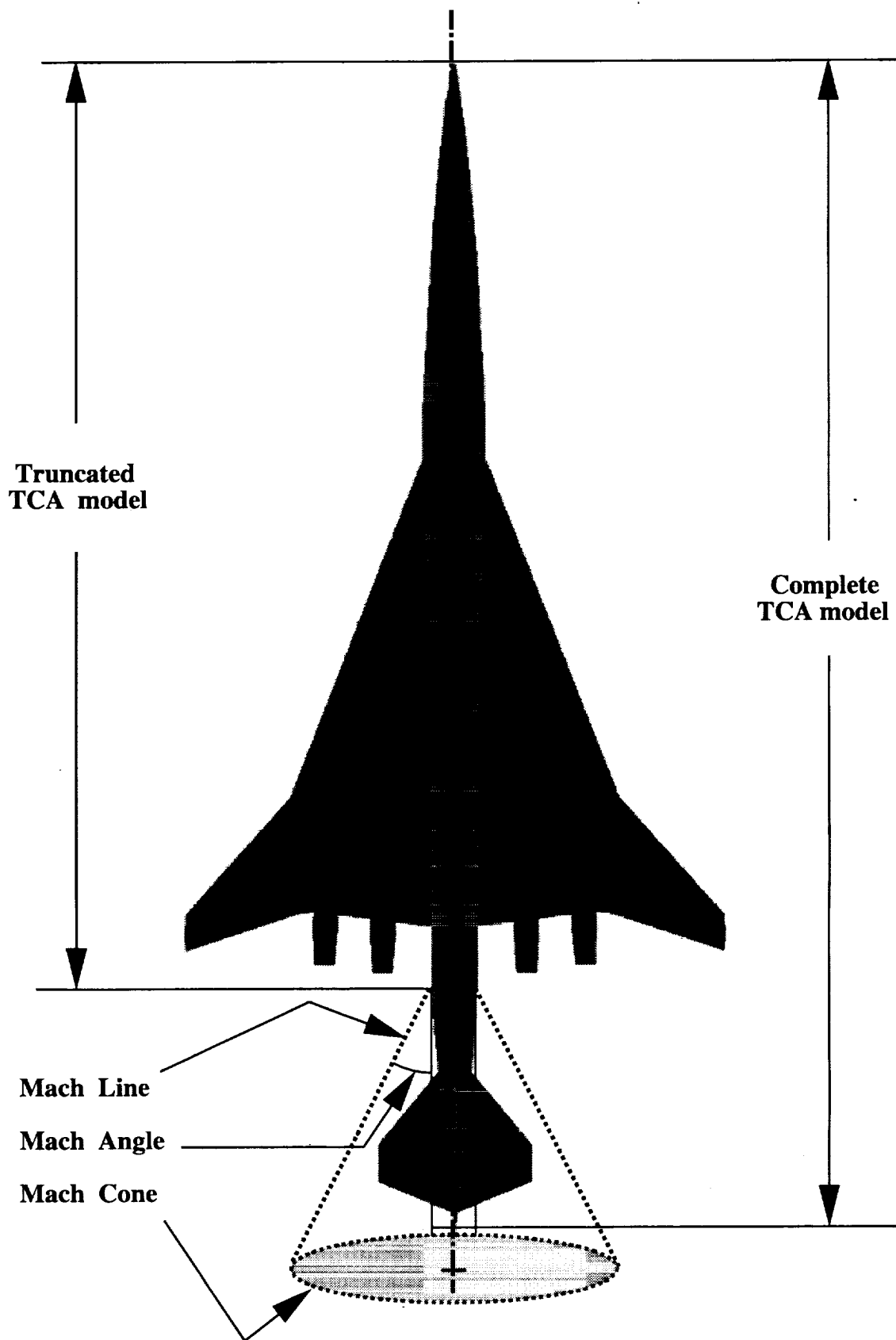


(a) Lower-surface view.

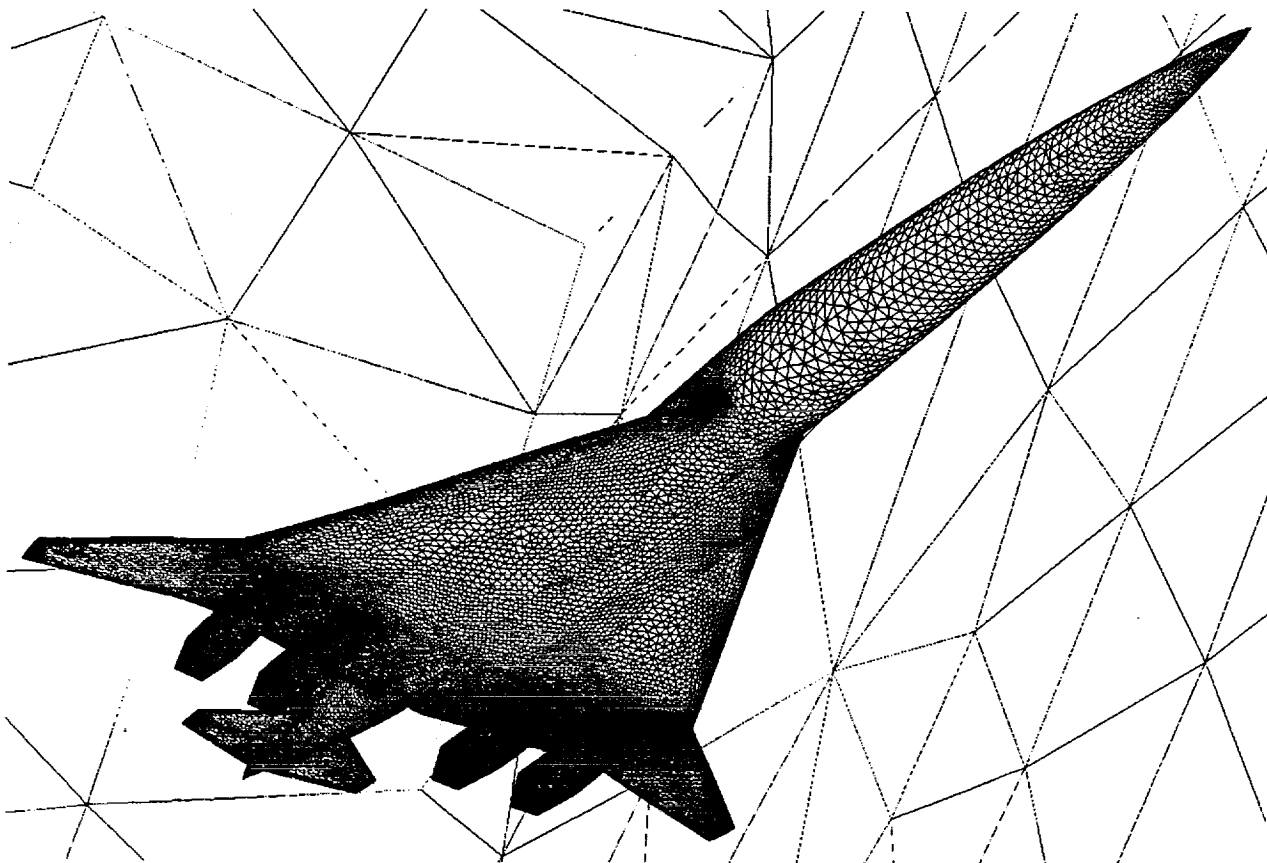


(b) Upper-surface view.

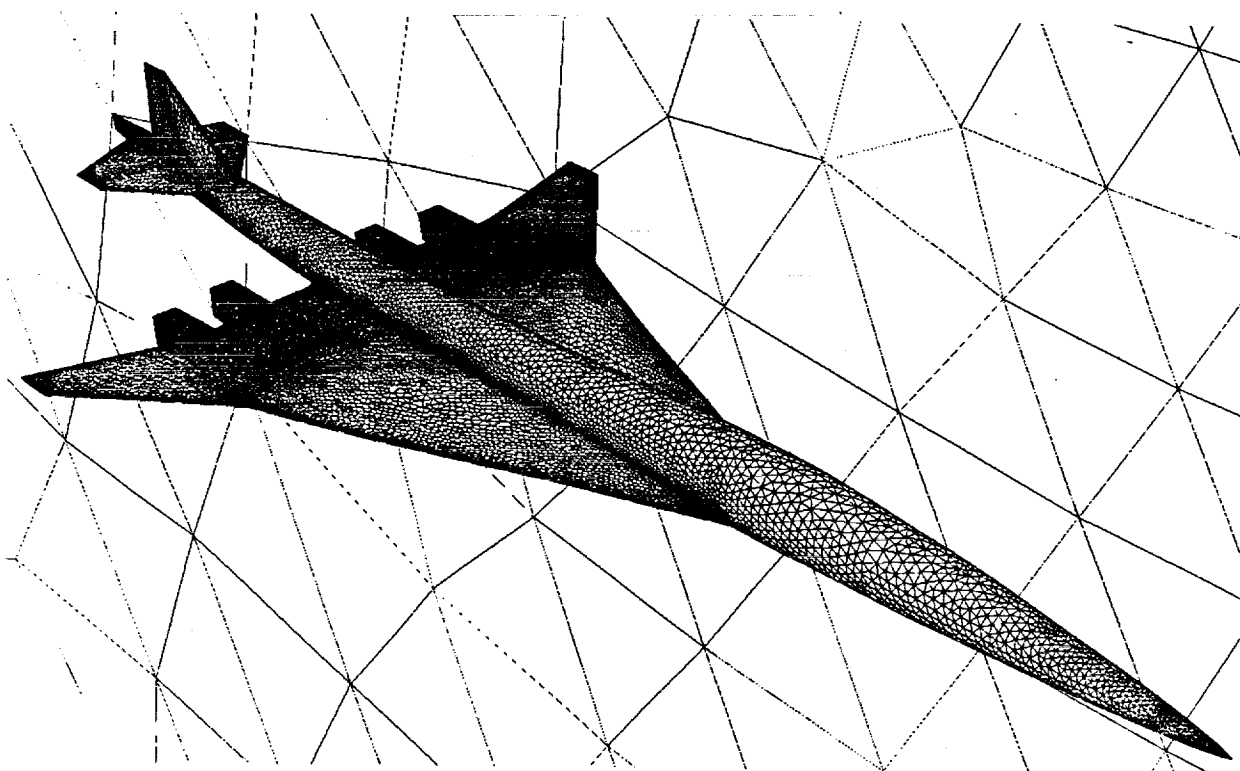
Figure 2. Computational solid surface model for the complete TCA.



3. Complete TCA solid model planform and the corresponding Mach cone for the truncated aft-fuselage/empennage.

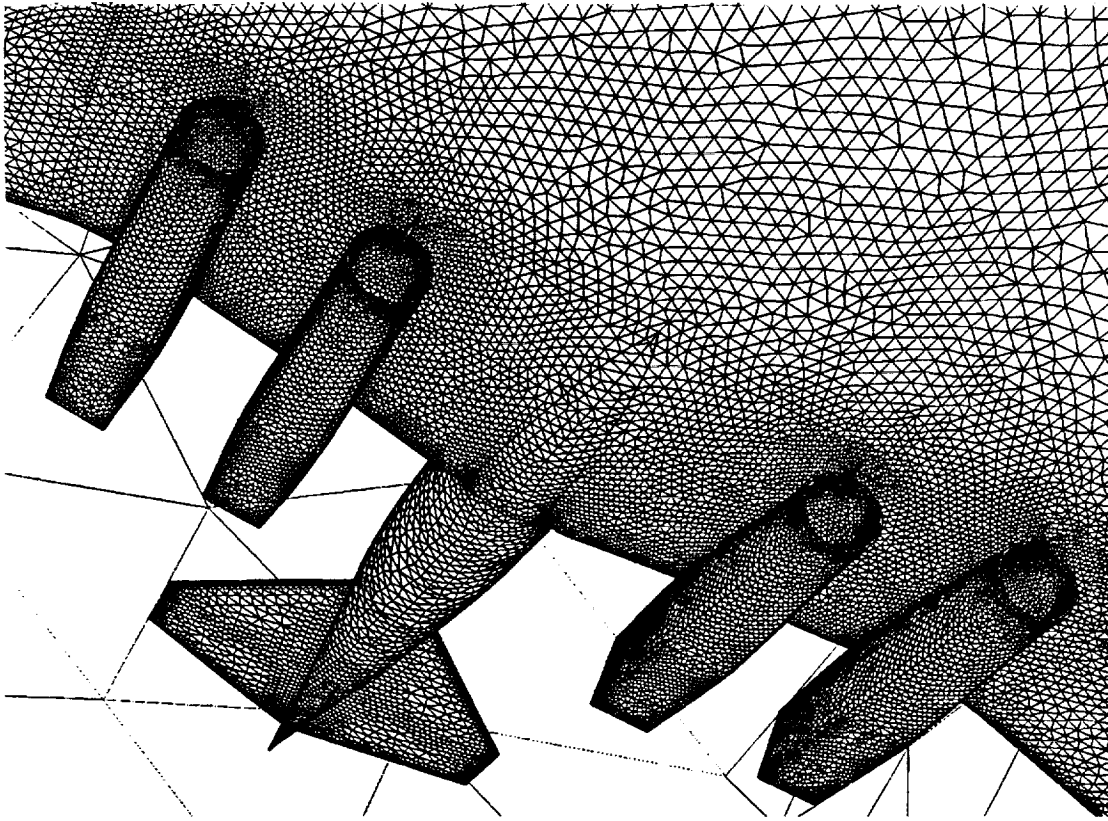


(a) Lower-surface.

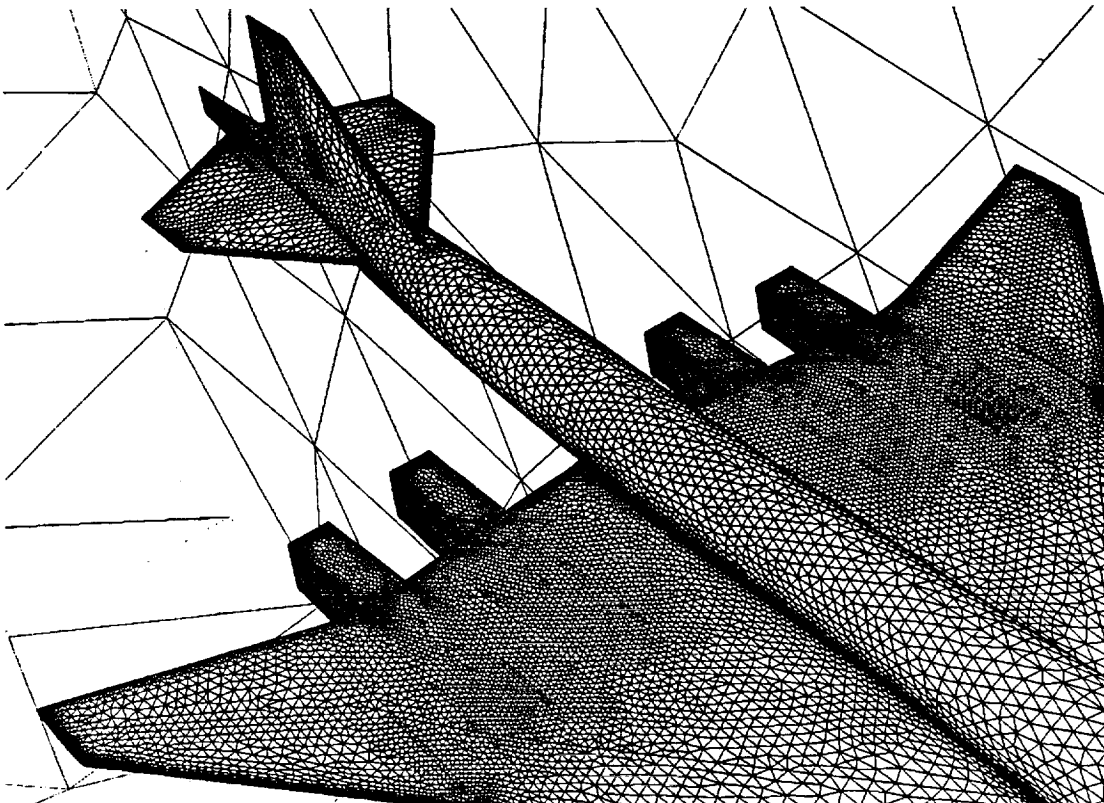


(b) Upper-surface.

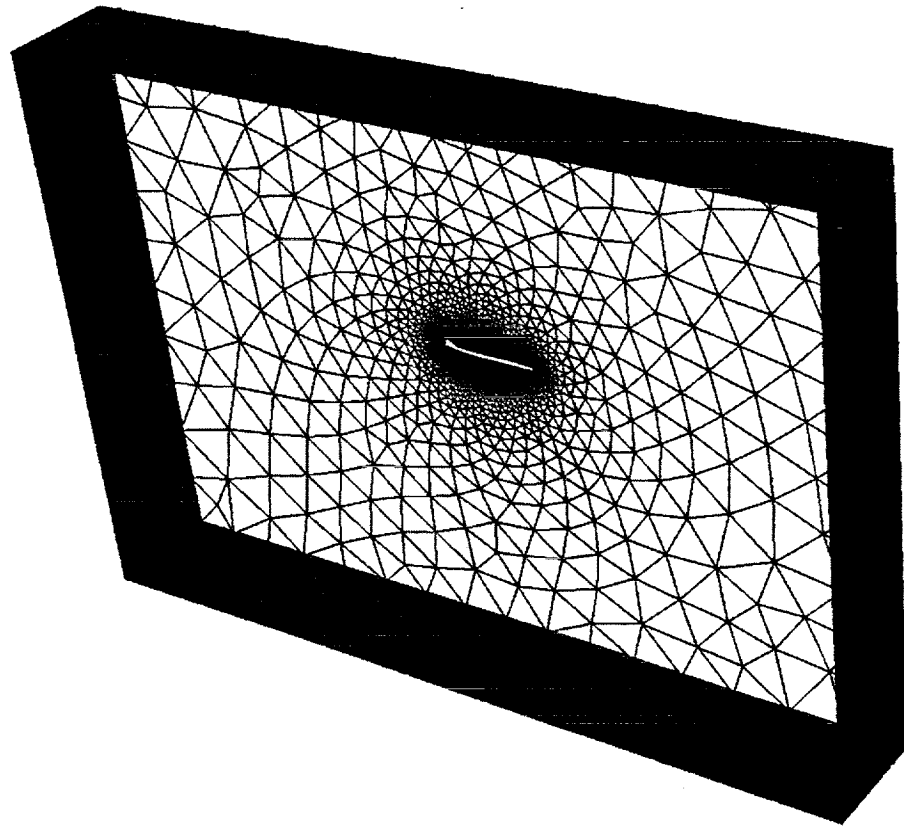
Figure 4. Computational surface grids.



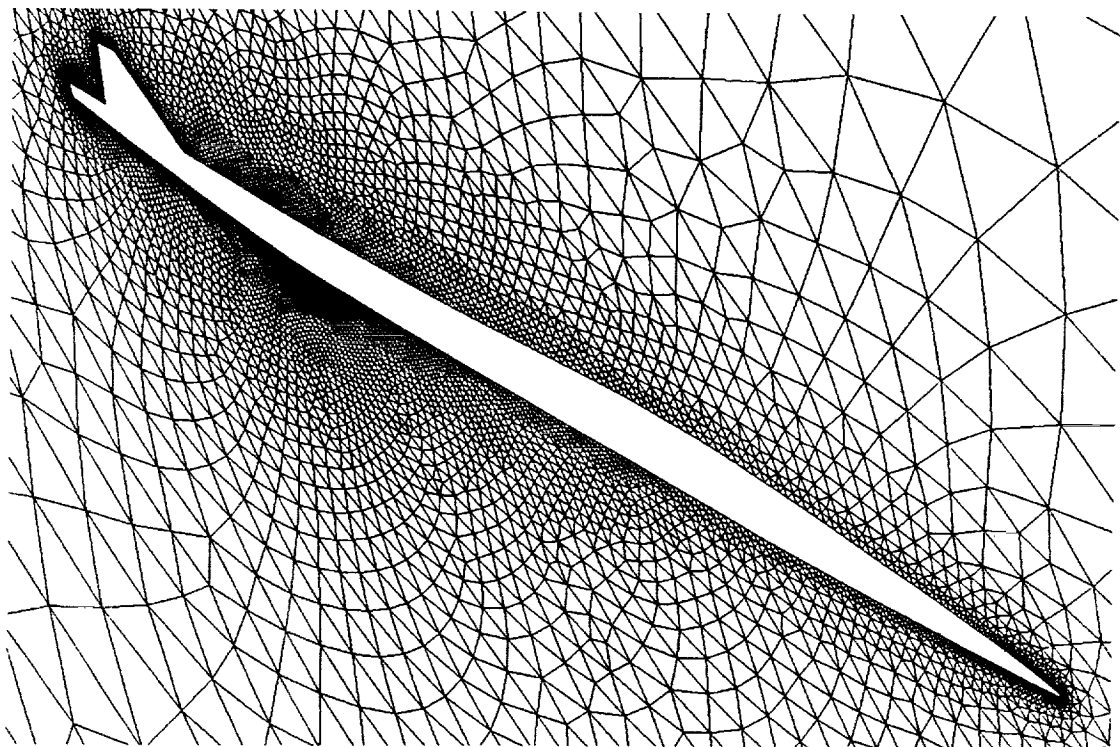
(c) Lower-surface close-up view.



(d) Upper-surface close-up view.
Figure 4. Concluded.

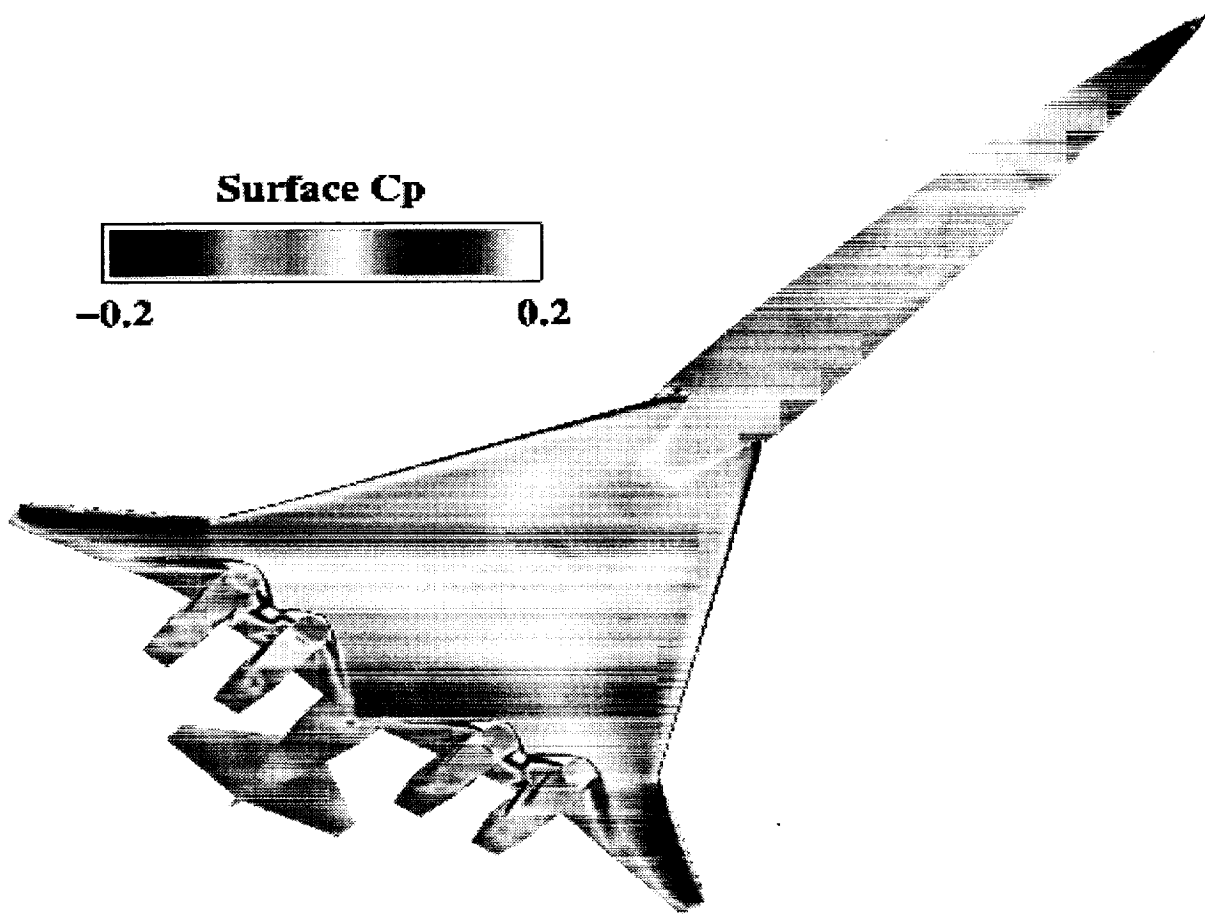


(a) Overall farfield boundaries.

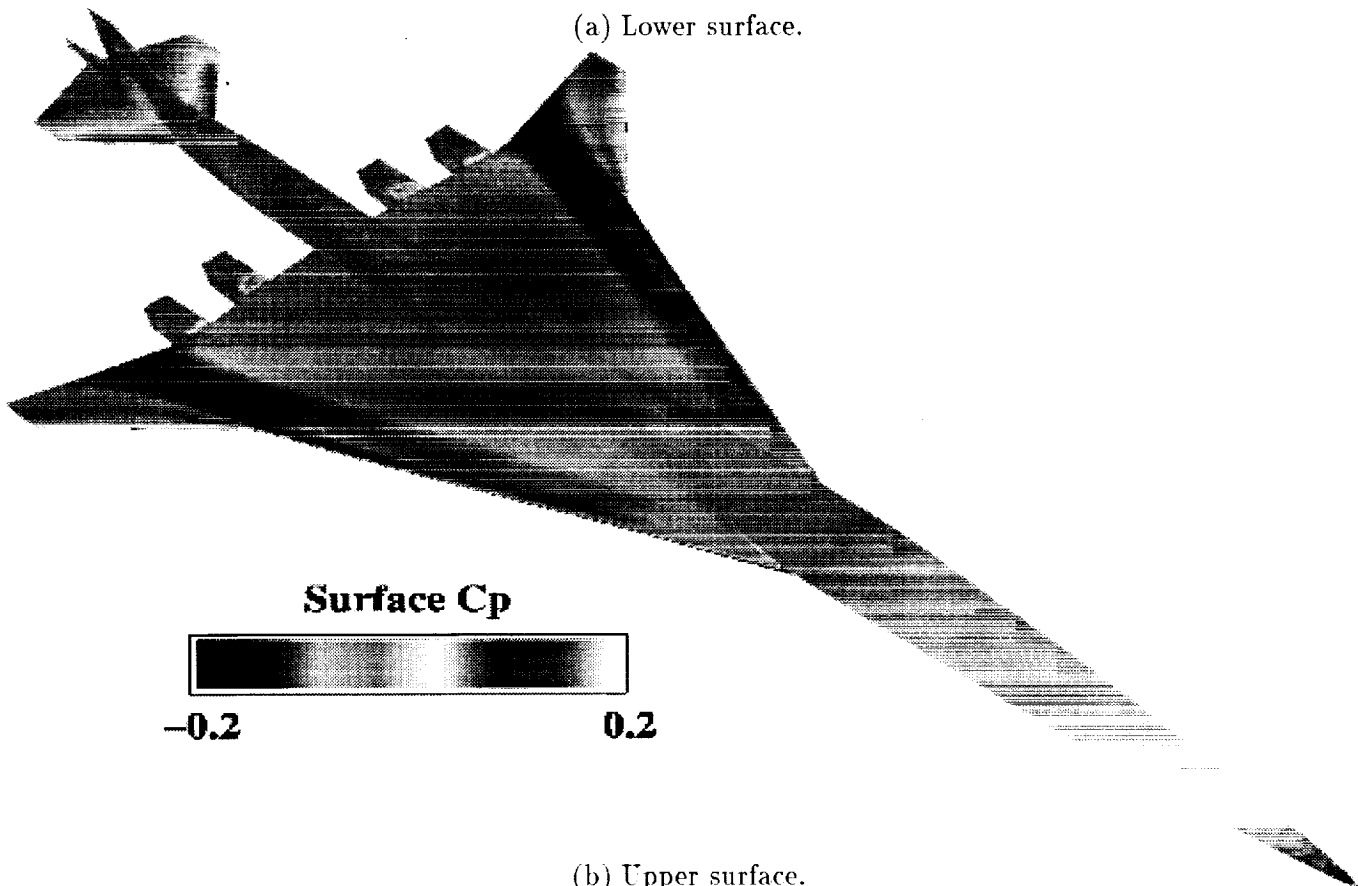


(b) Close-up view of the grids in the plane-of-symmetry.

Figure 5. Computational domain and plane-of-symmetry grids.

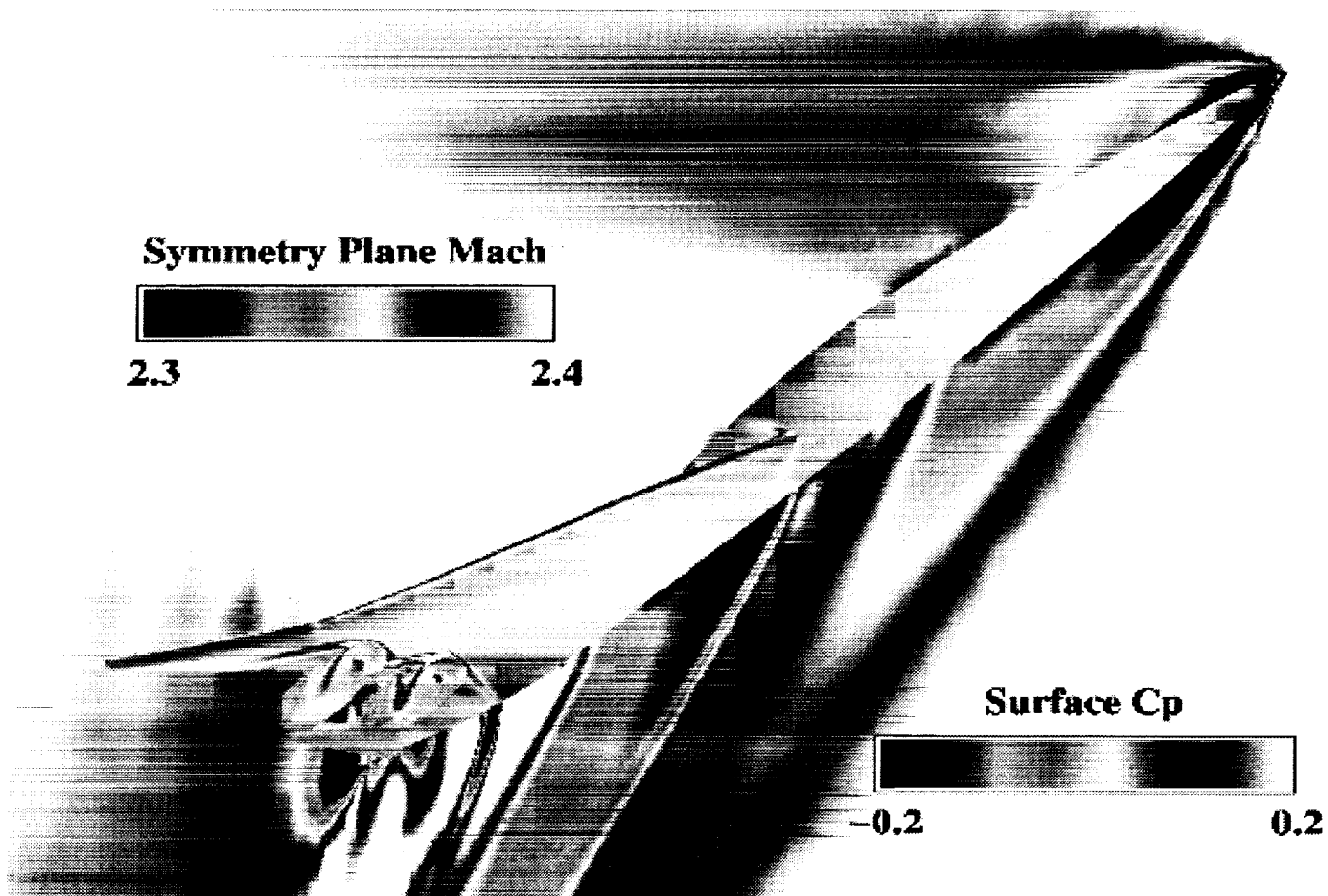


(a) Lower surface.

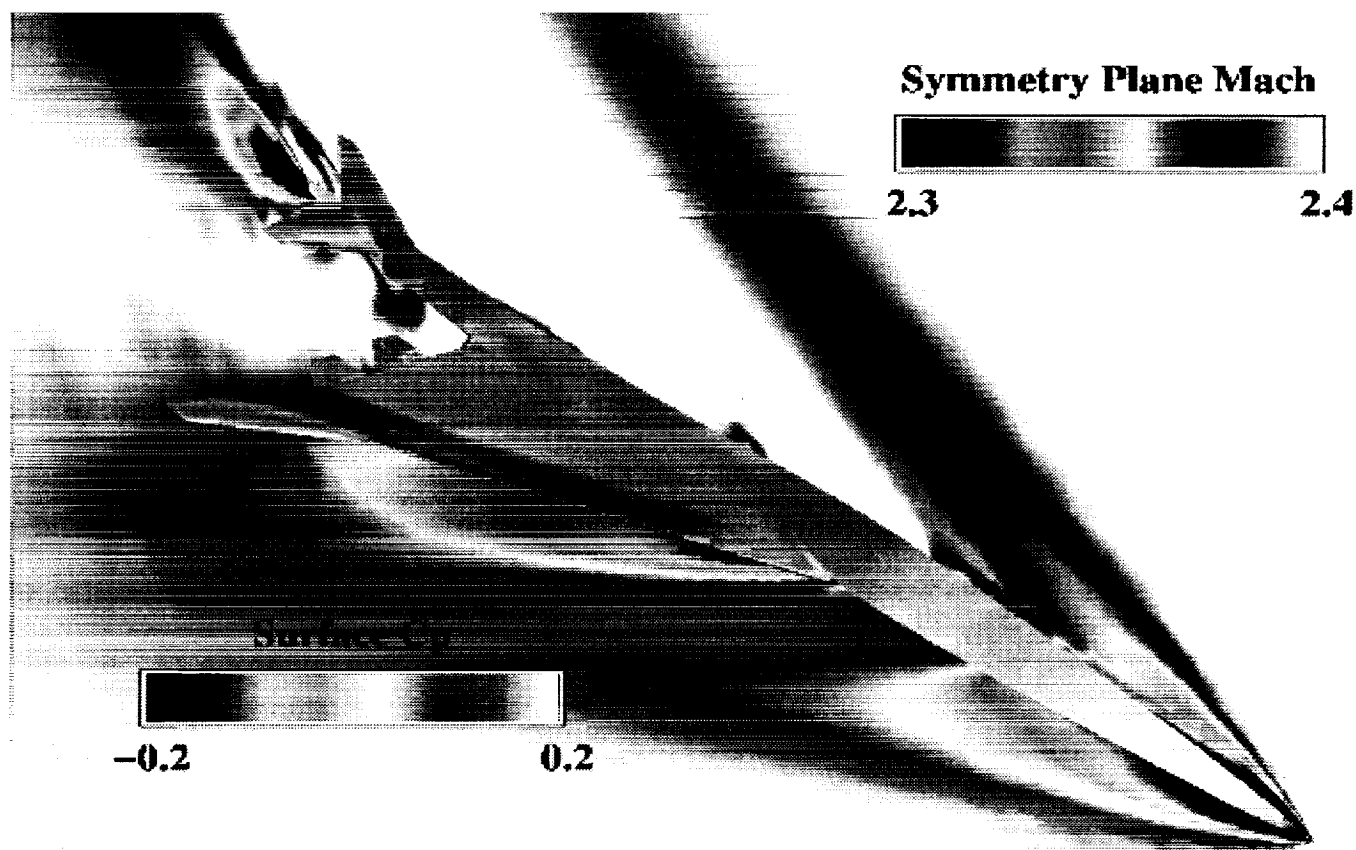


(b) Upper surface.

Figure 6. Computed surface C_p contours - $\alpha = 3.5^\circ$, $M_\infty = 2.4$, $\beta = 0^\circ$.

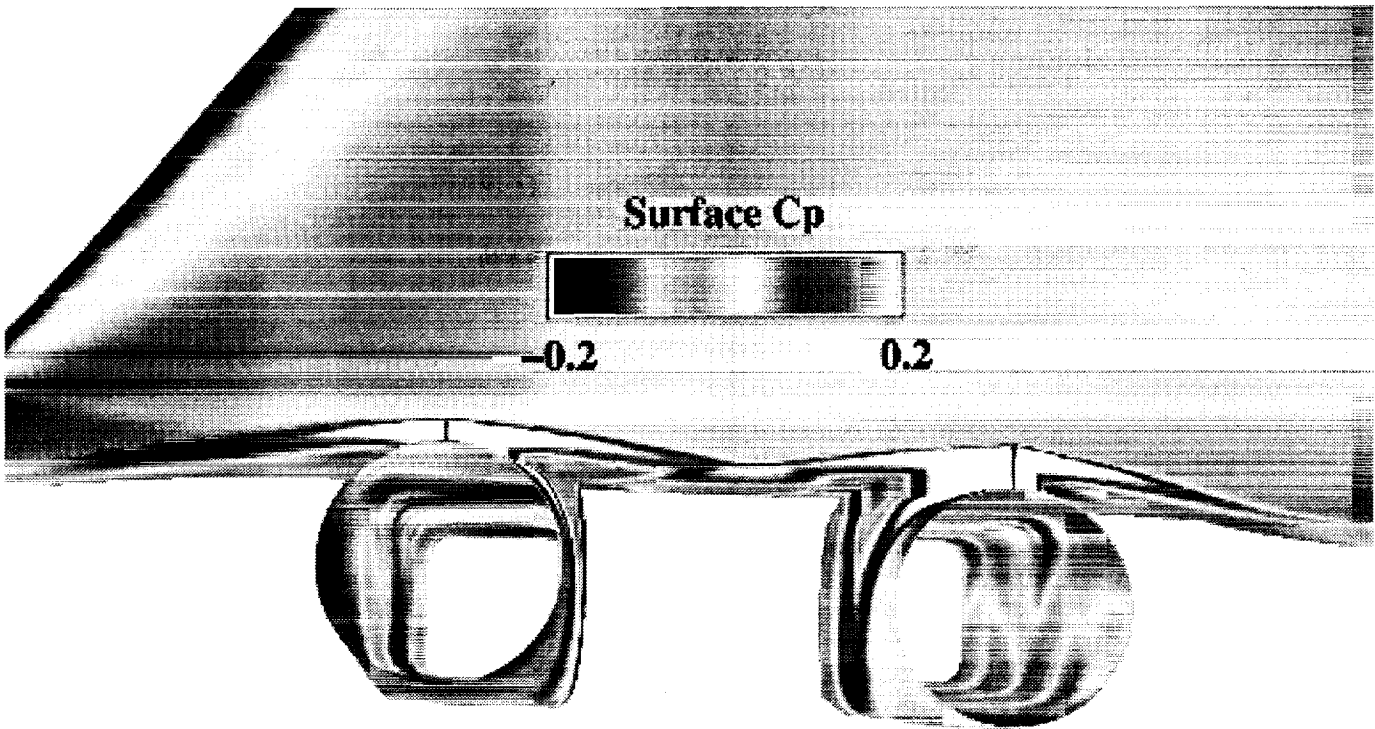


(a) Lower surface.

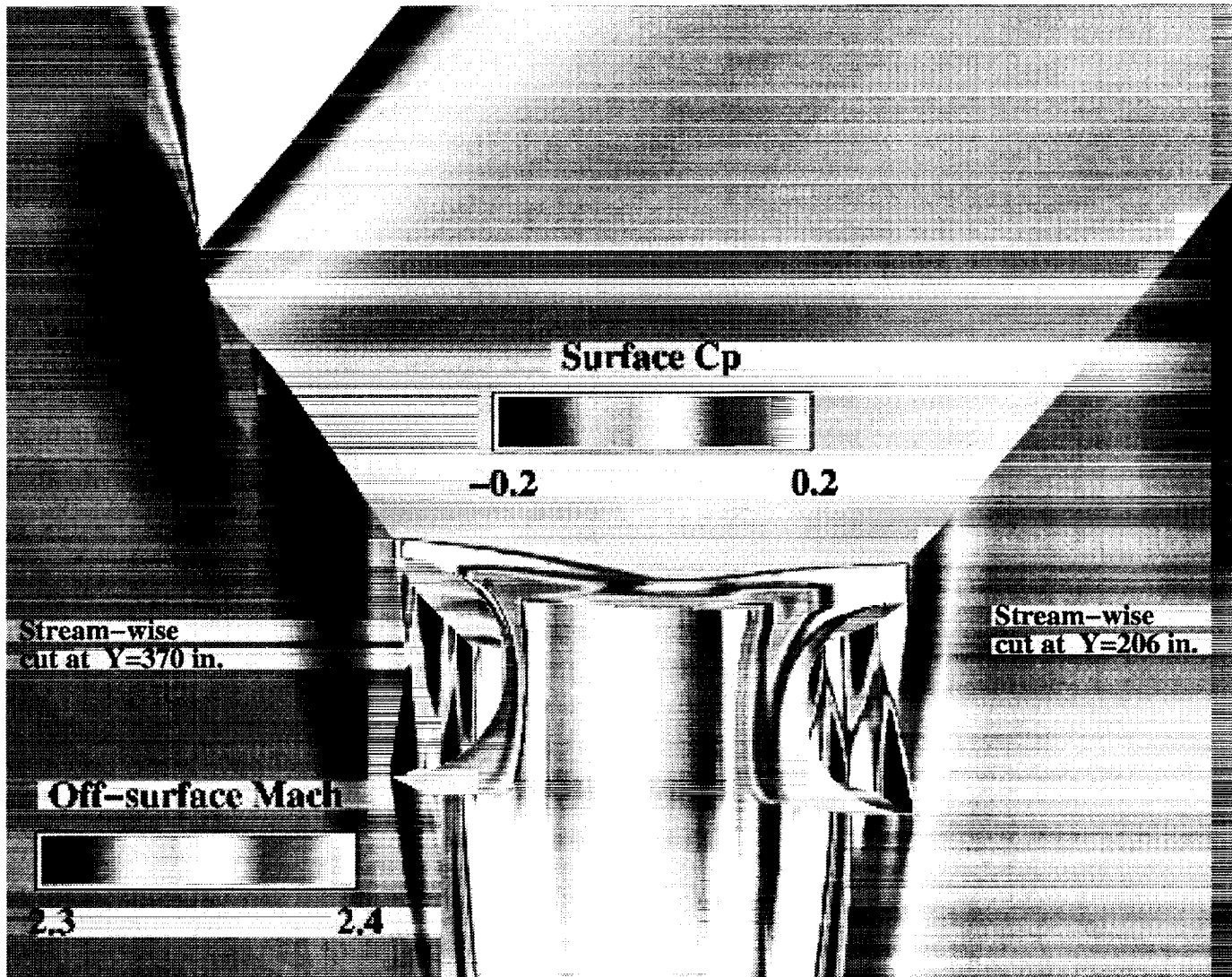


(b) Upper surface.

Figure 7. Computed surface C_p and Mach variation in the plane-of-symmetry. $\alpha = 3.5^\circ$, $M_\infty = 2.4$, $\beta = 0$



(a) Surface C_p .



(b) Surface C_p and off-surface Mach variation.

Figure 8. Close-up view of the nacelle's computed flow characteristics. $\alpha = 3.5^\circ$, $M_\infty = 2.4$, $\beta = 0^\circ$.

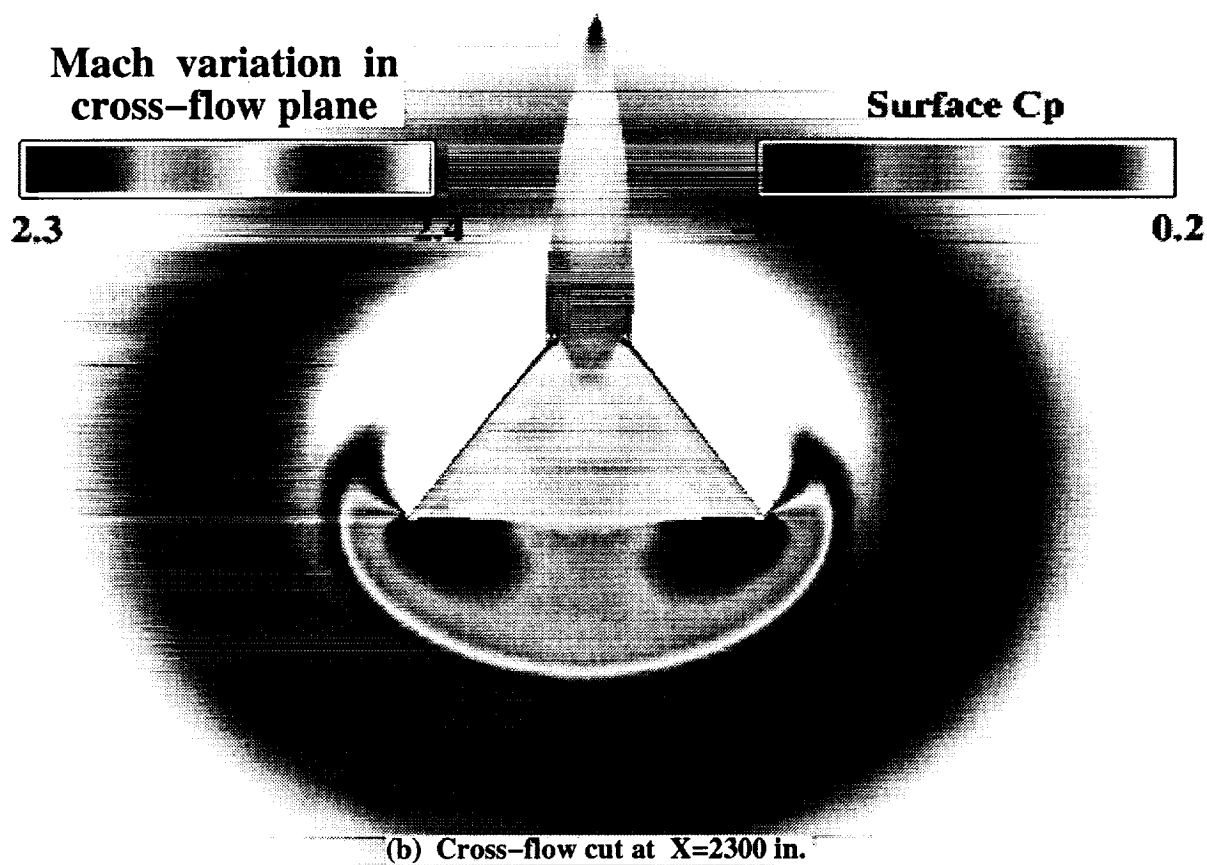


Figure 9. Computed surface C_p and Mach variation in cross-flow planes. $\alpha = 3.5^\circ$, $M_\infty = 2.4$, $\beta = 0^\circ$.

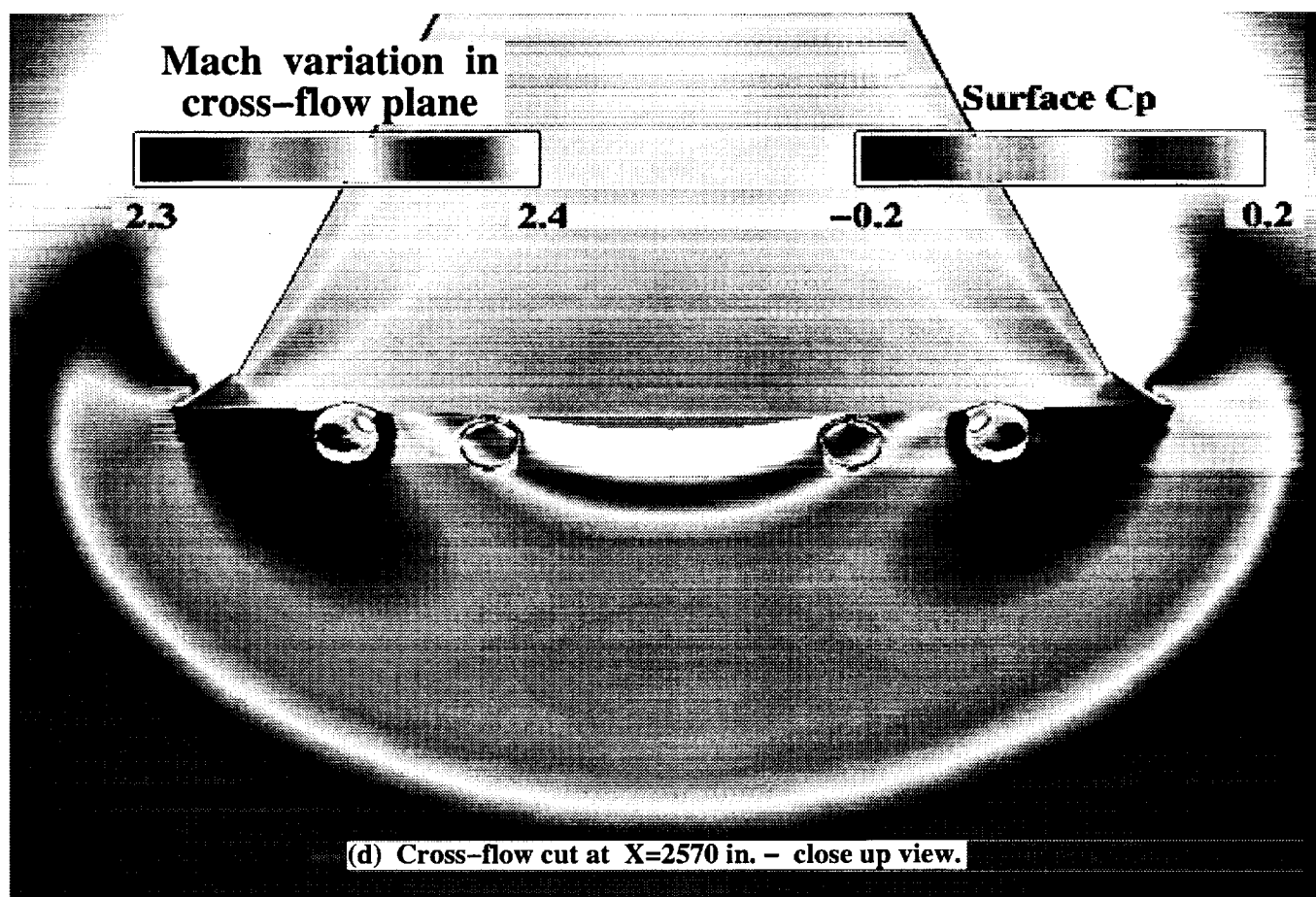


Figure 9. Continued.

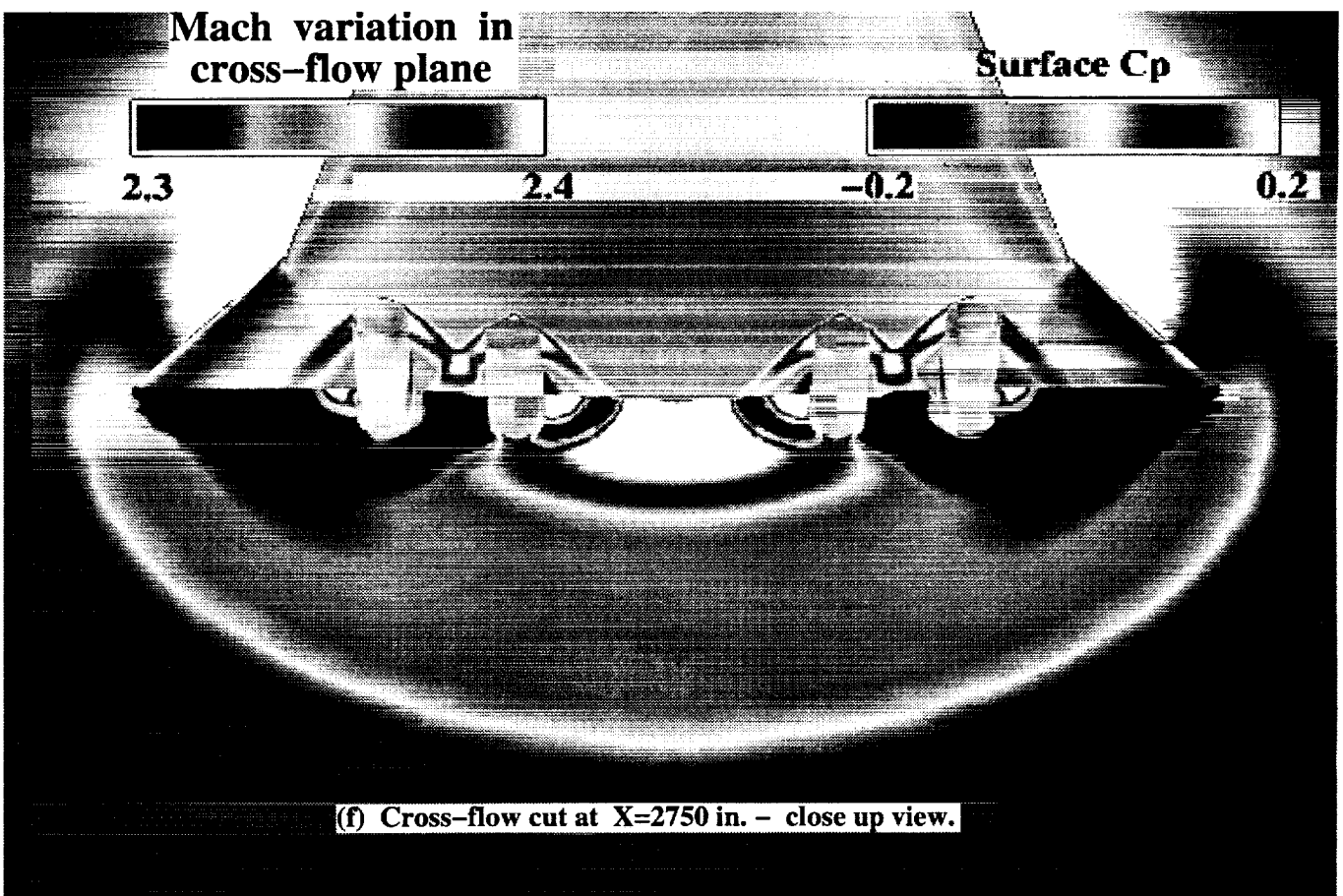
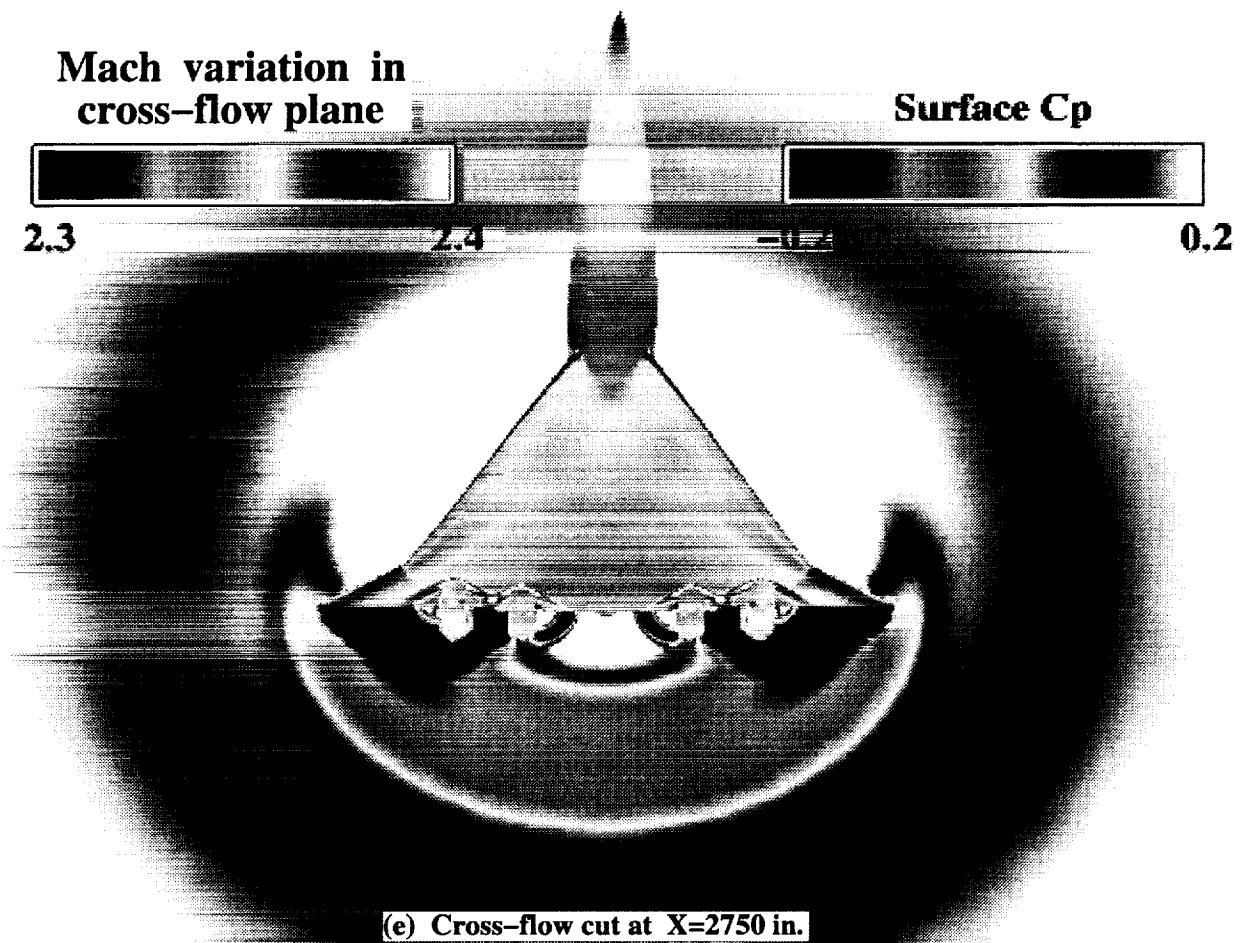


Figure 9. Continued.

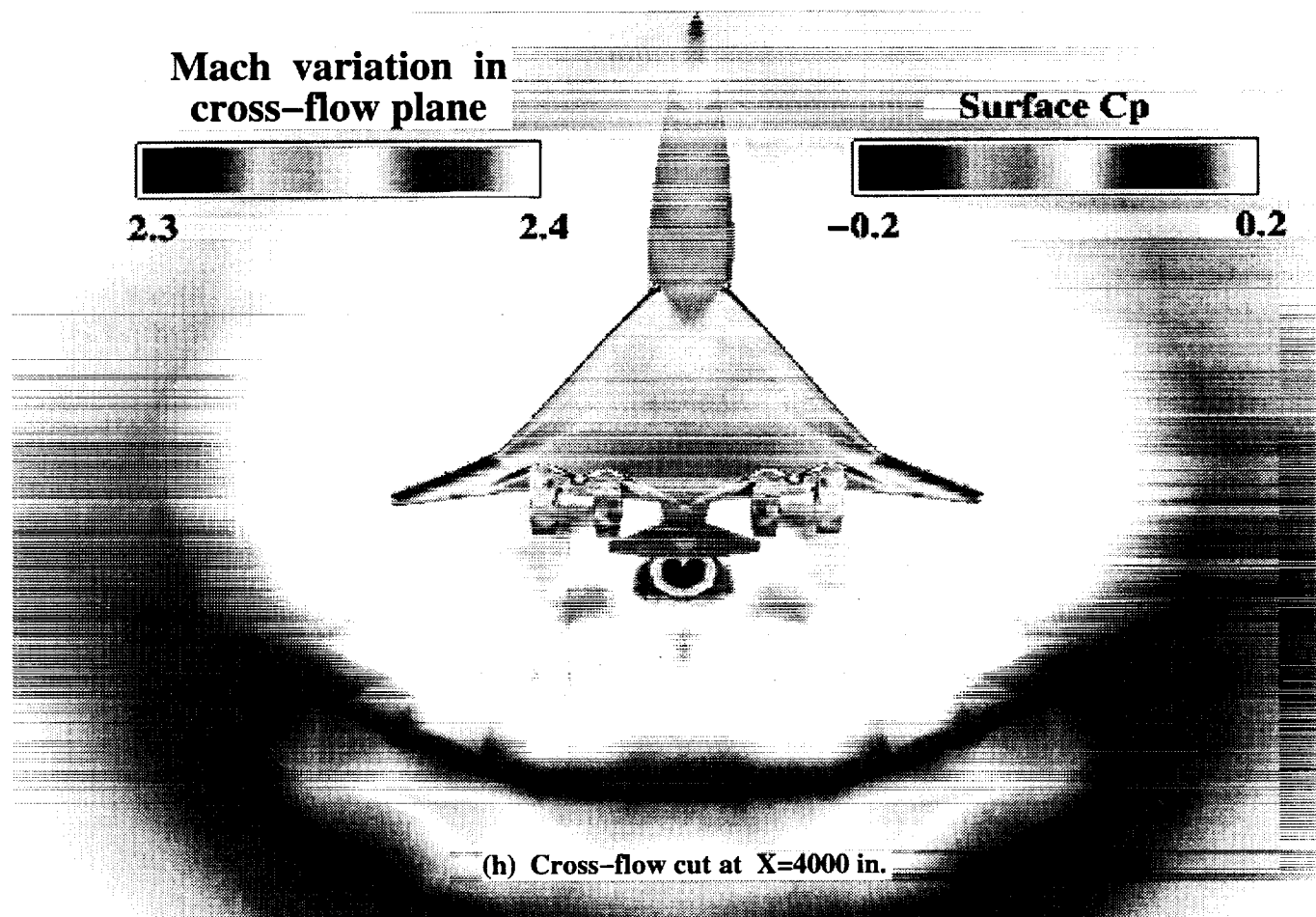
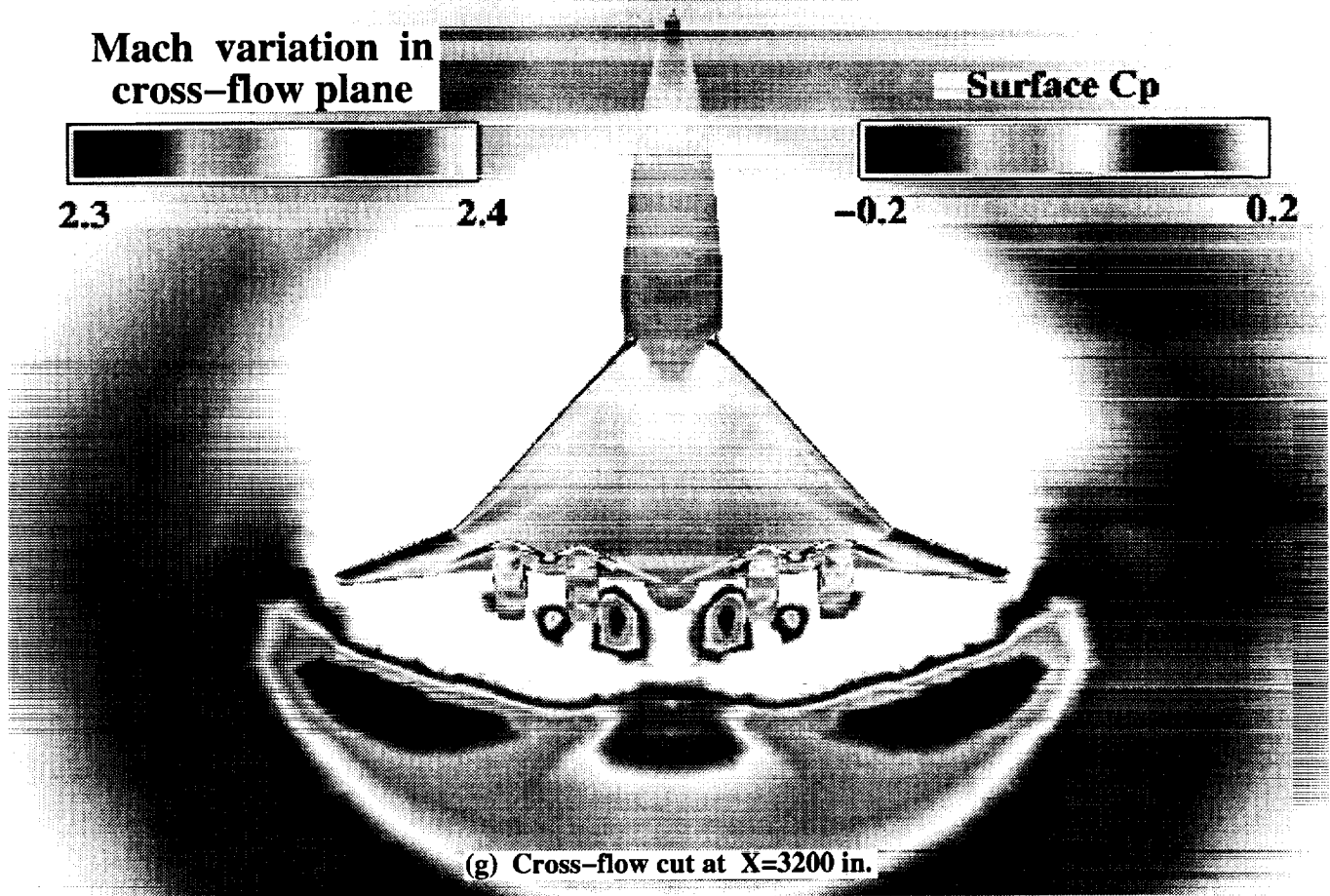


Figure 9. Concluded.

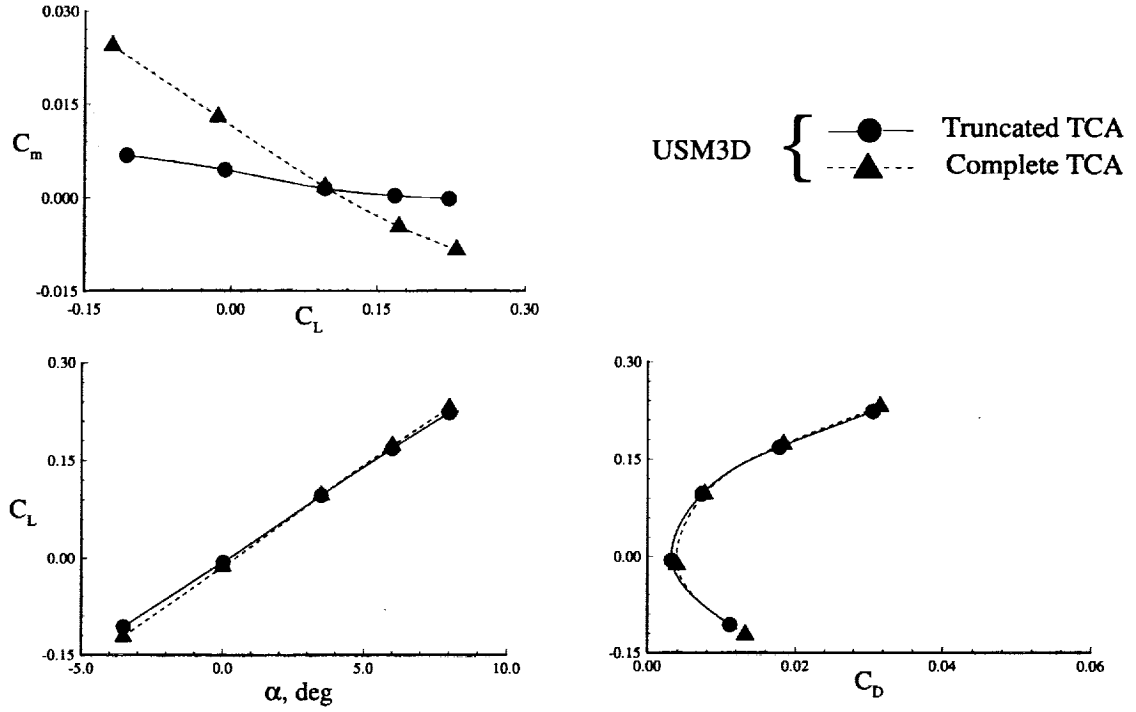


Figure 10. Computed longitudinal aerodynamic characteristics. $M_\infty = 2.4$, $\beta = 0^\circ$.

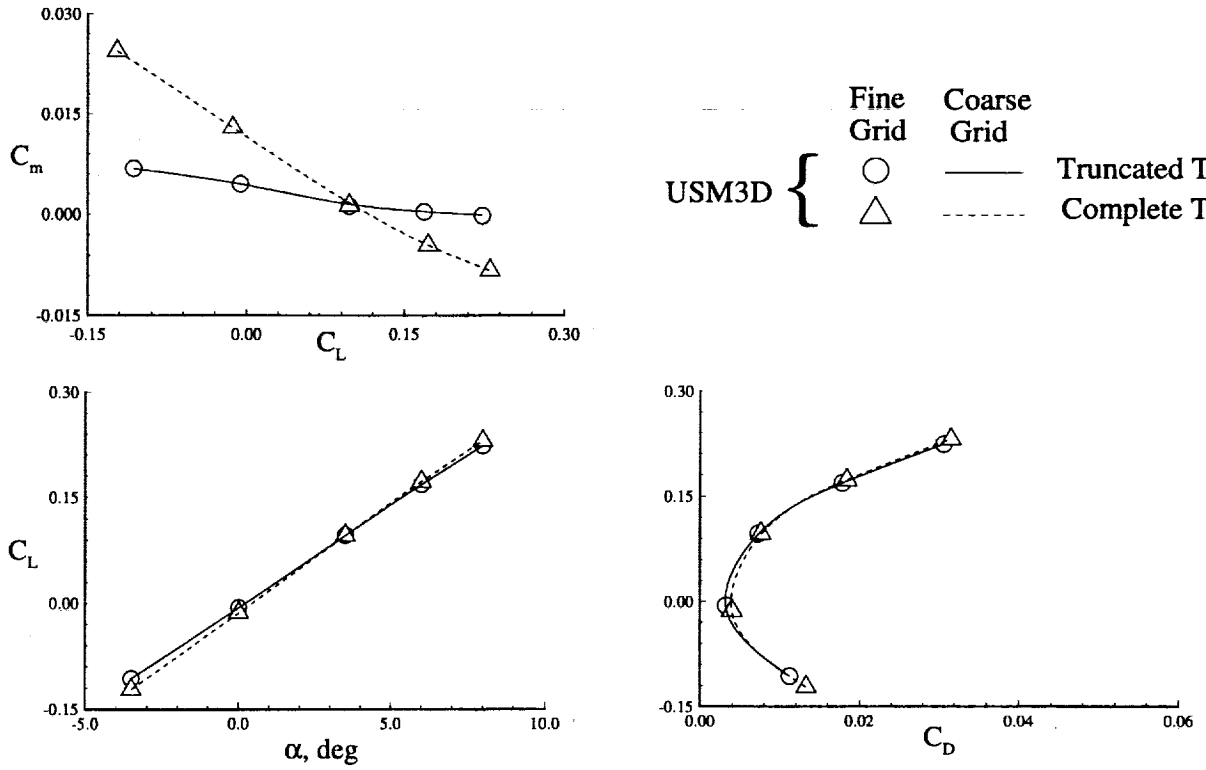


Figure 11. Grid refinement sensitivity on computed longitudinal aerodynamic characteristics. $M_\infty = 2.4$, $\beta = 0^\circ$.

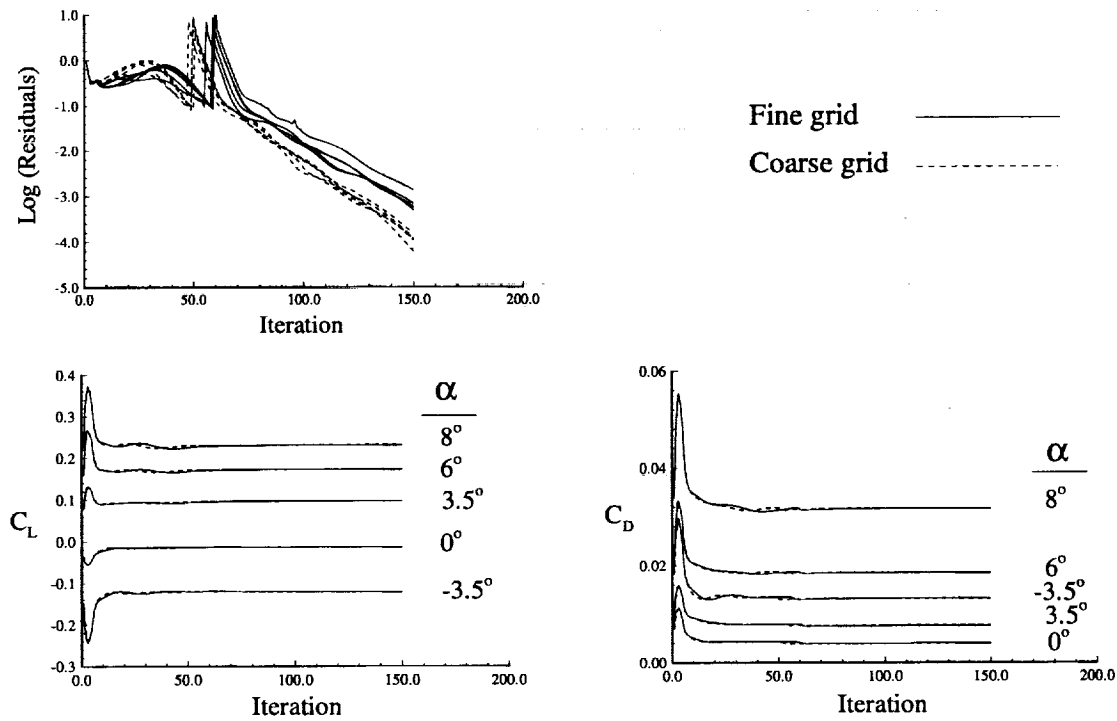
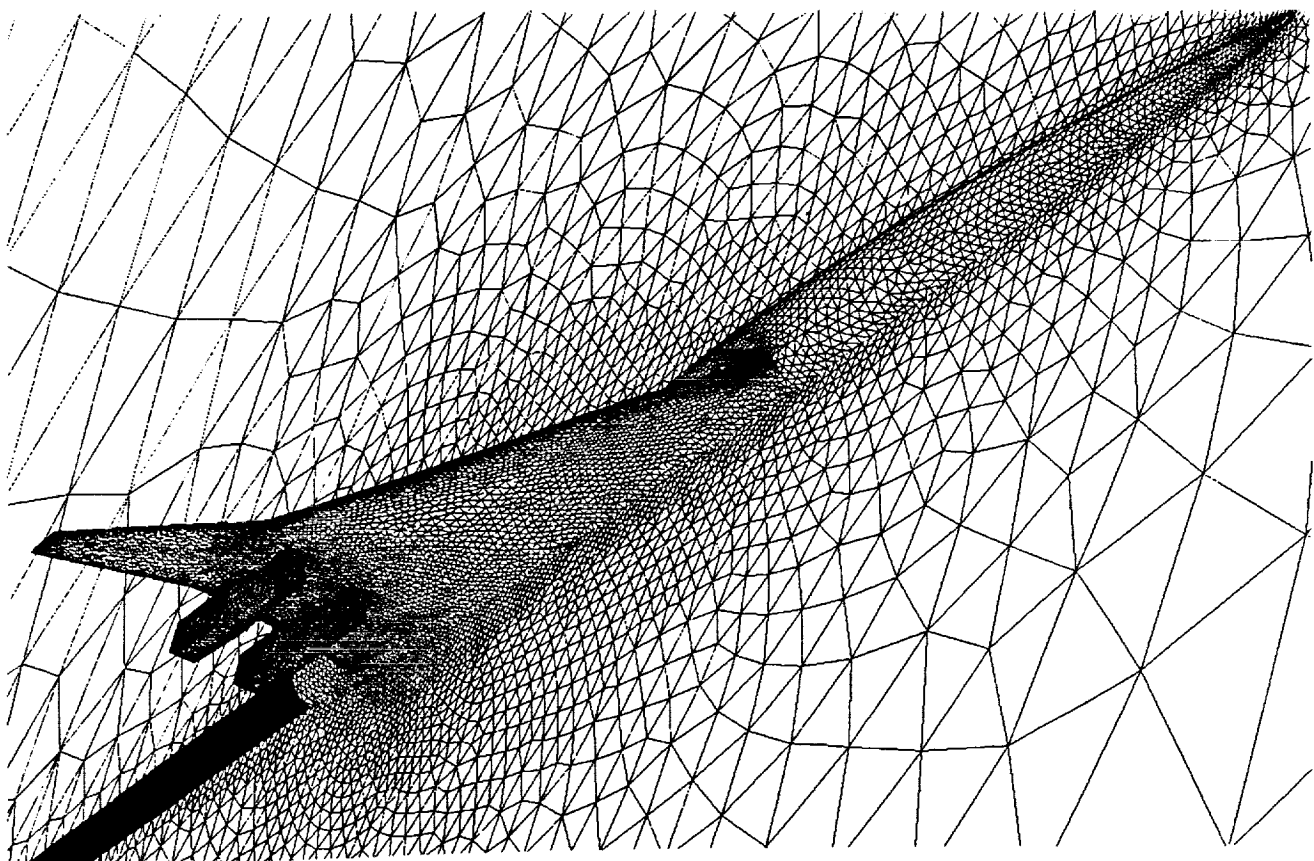
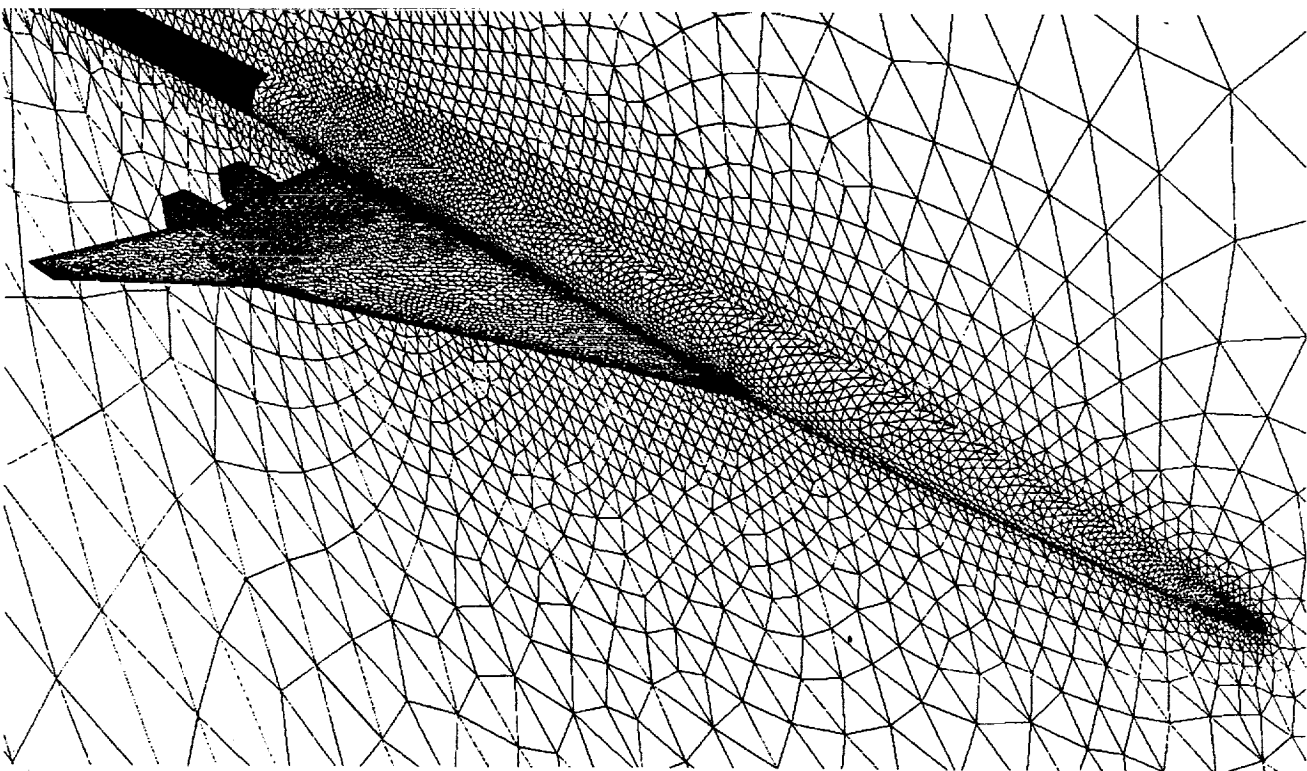


Figure 12. Solution convergence characteristics for different angles-of-attack and grids. $M_\infty = 2.4$, $\beta = 0^\circ$.



(a) Lower-surface.



(b) Upper-surface.

Figure 13. Computational grids on the surface and plane-of-symmetry for the truncated TCA configuration.

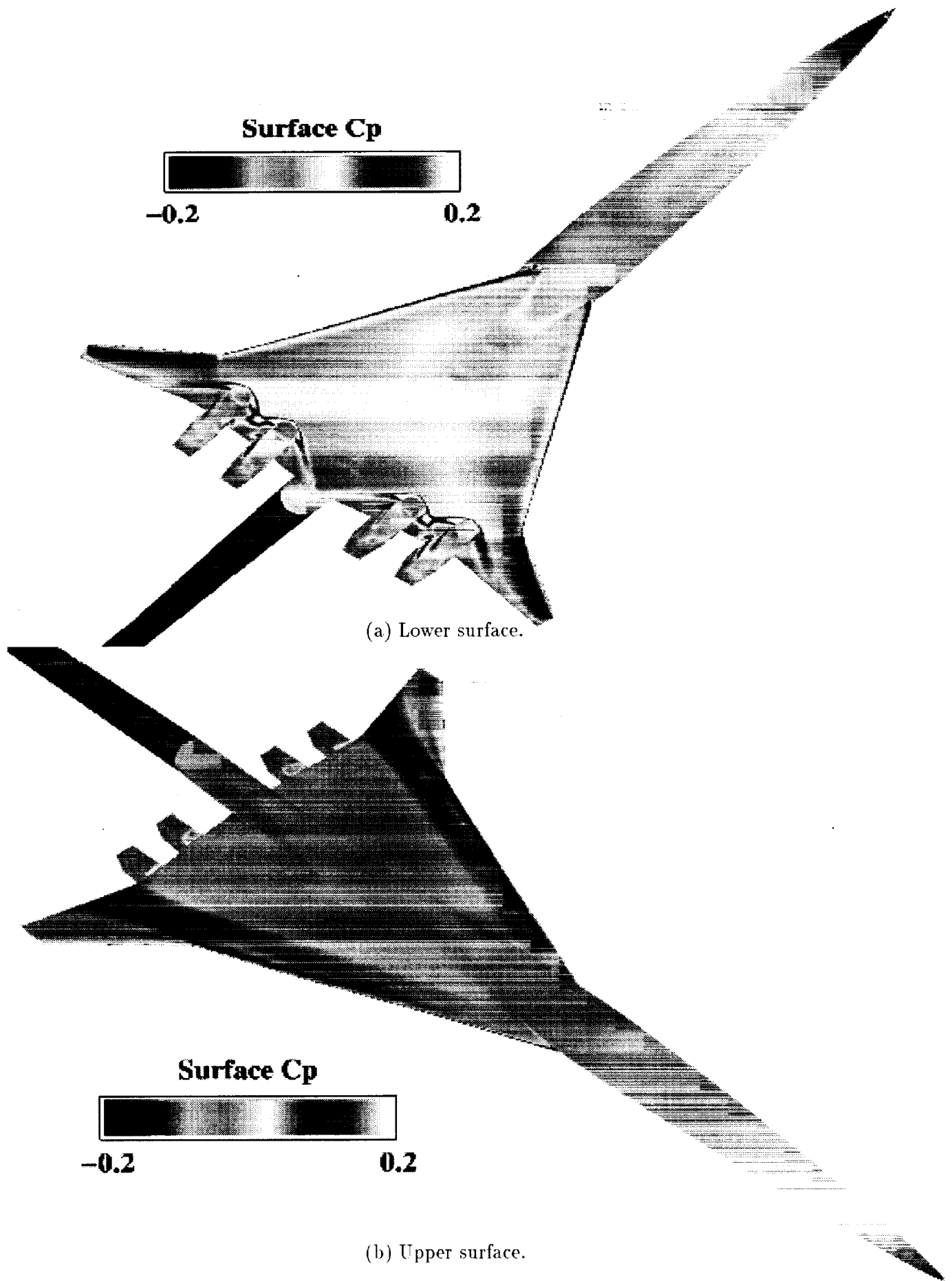


Figure 14. Computed surface C_p for the truncated TCA - $\alpha = 3.5^\circ$, $M_\infty = 2.4$, $\beta = 0^\circ$.

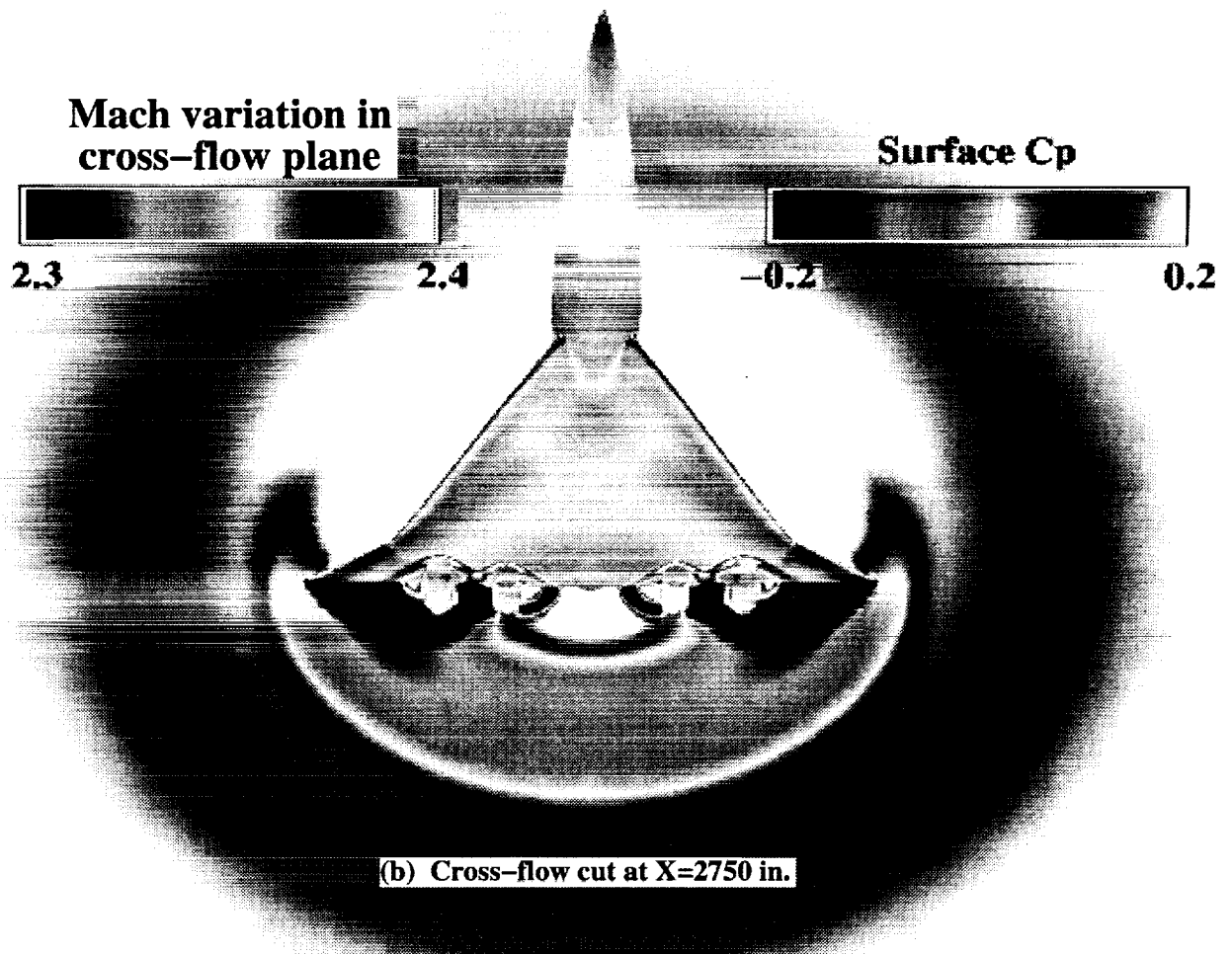
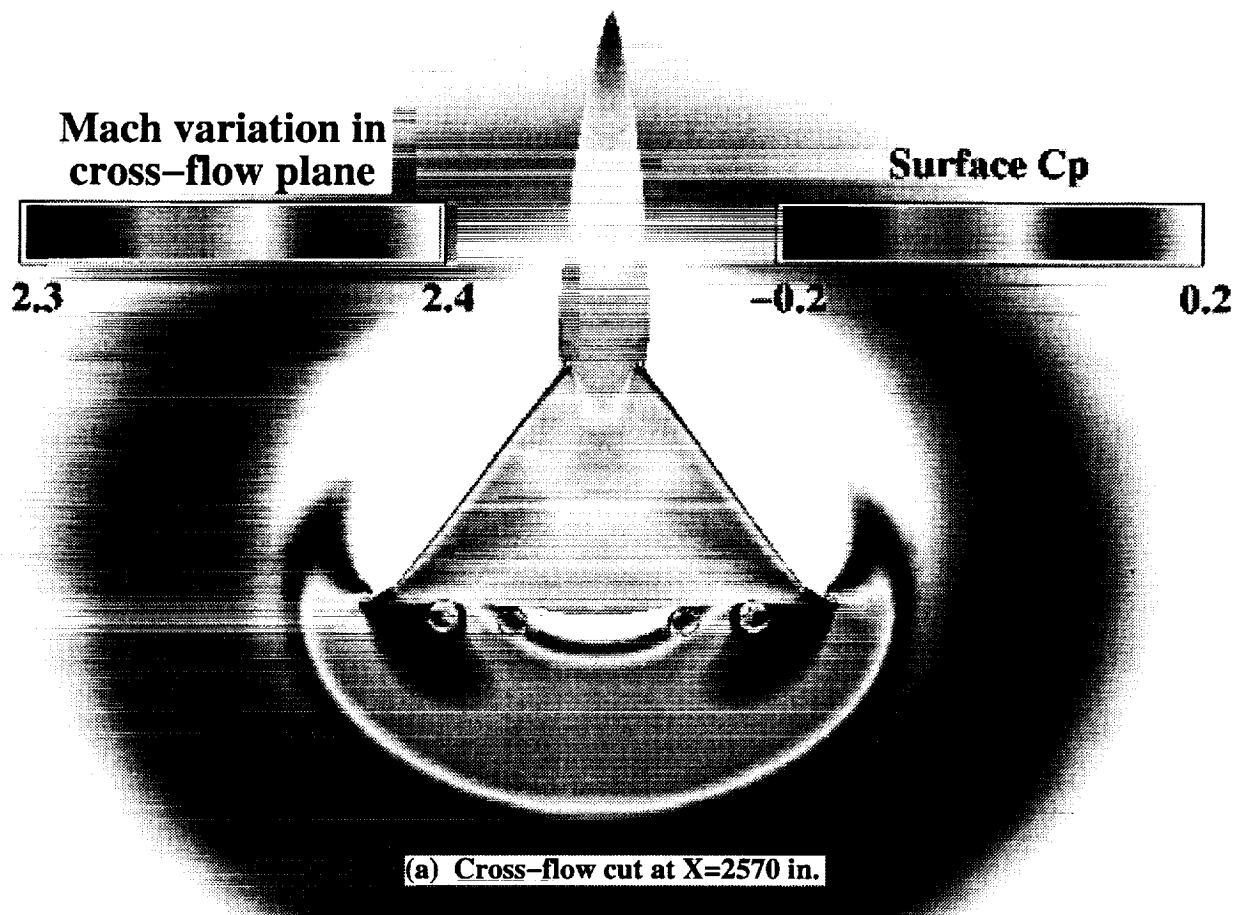


Figure 15. Truncated TCA computed surface C_p and Mach variation in cross-flow planes. $\alpha = 3.5^\circ$, $M_\infty = 2.4$, ℓ

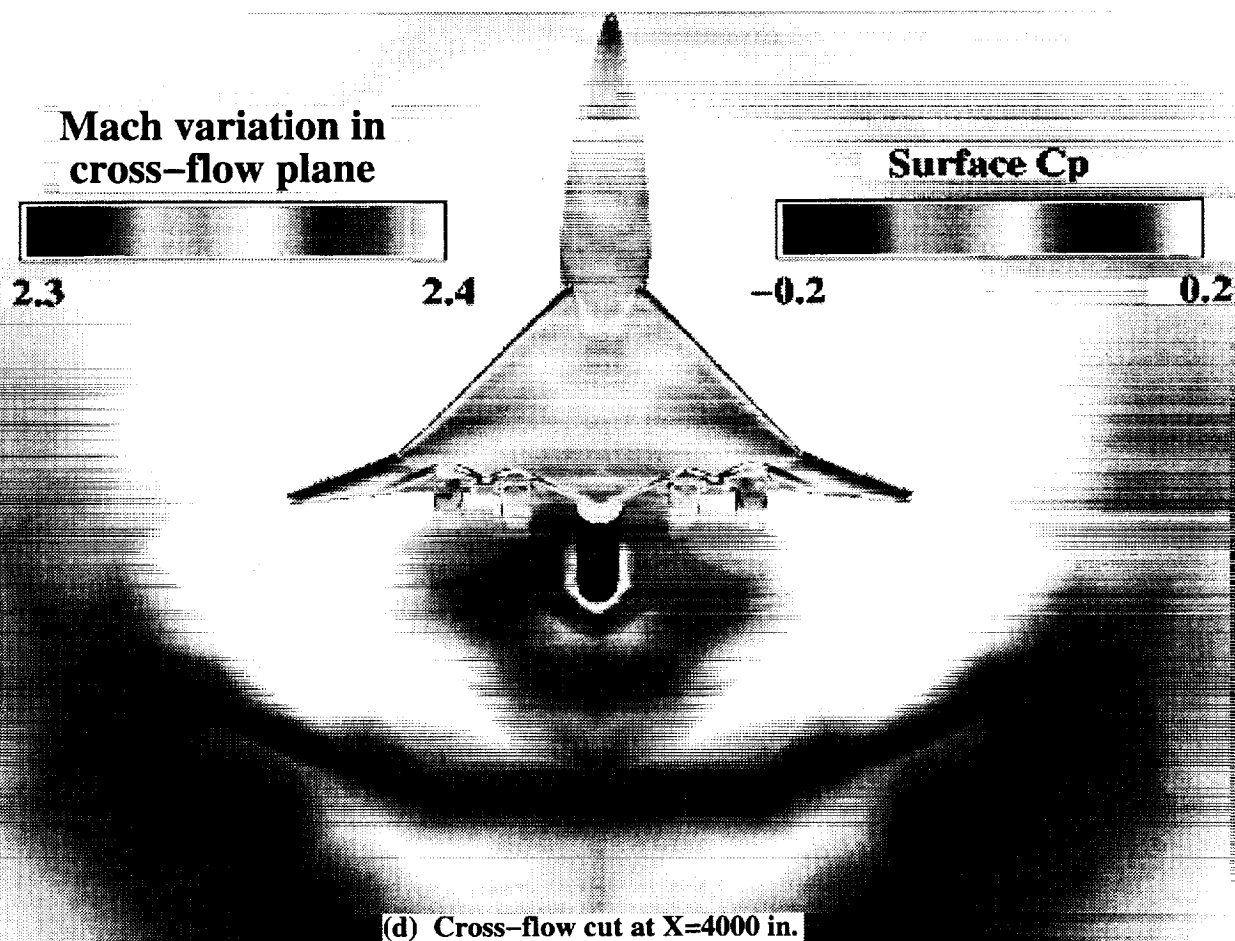
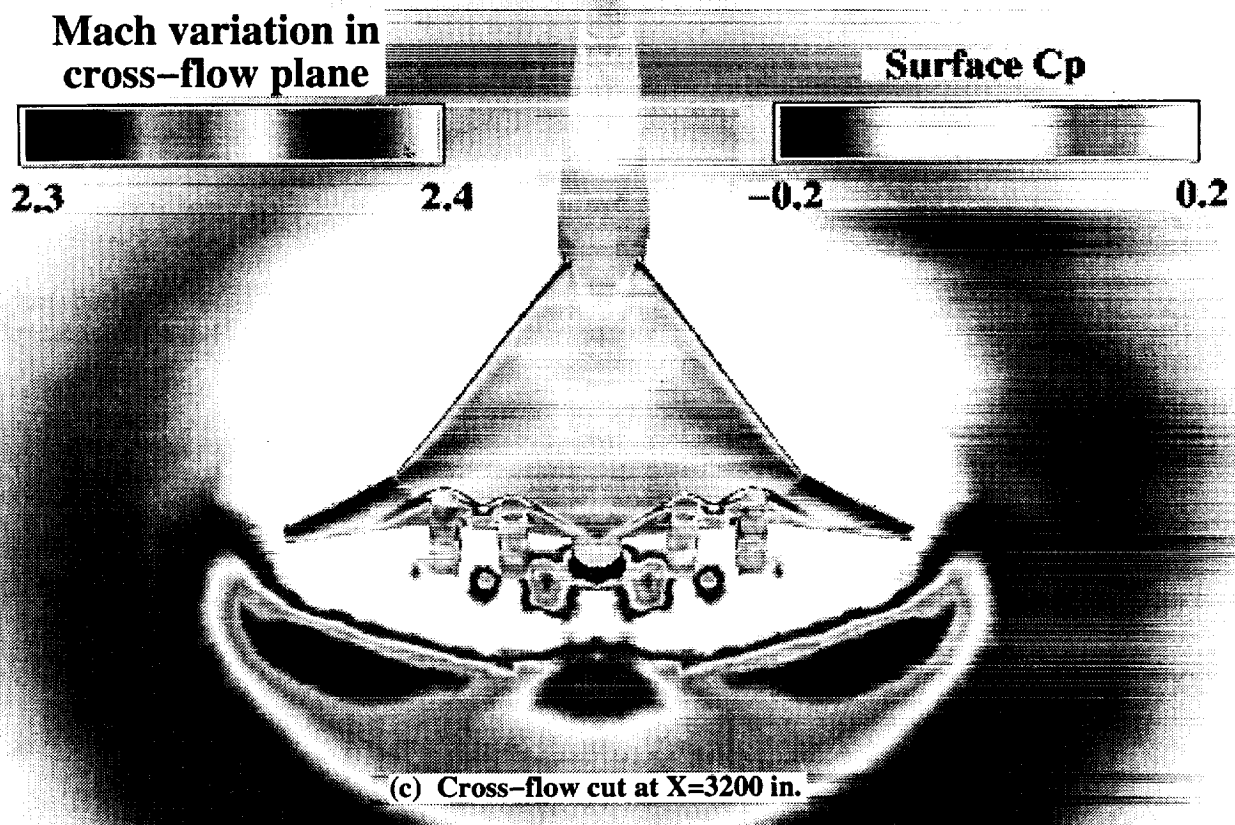


Figure 15. Concluded.

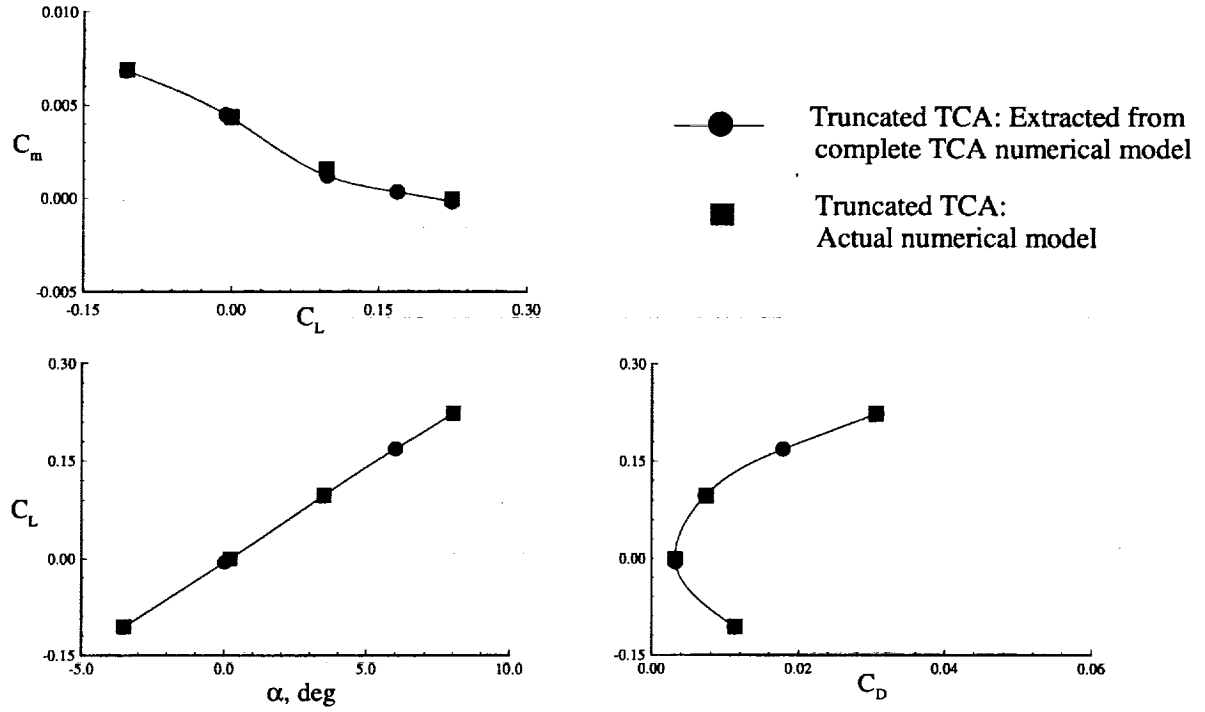


Figure 16. Truncated TCA computed longitudinal aerodynamic characteristics. $M_\infty = 2.4$, $\beta = 0^\circ$.

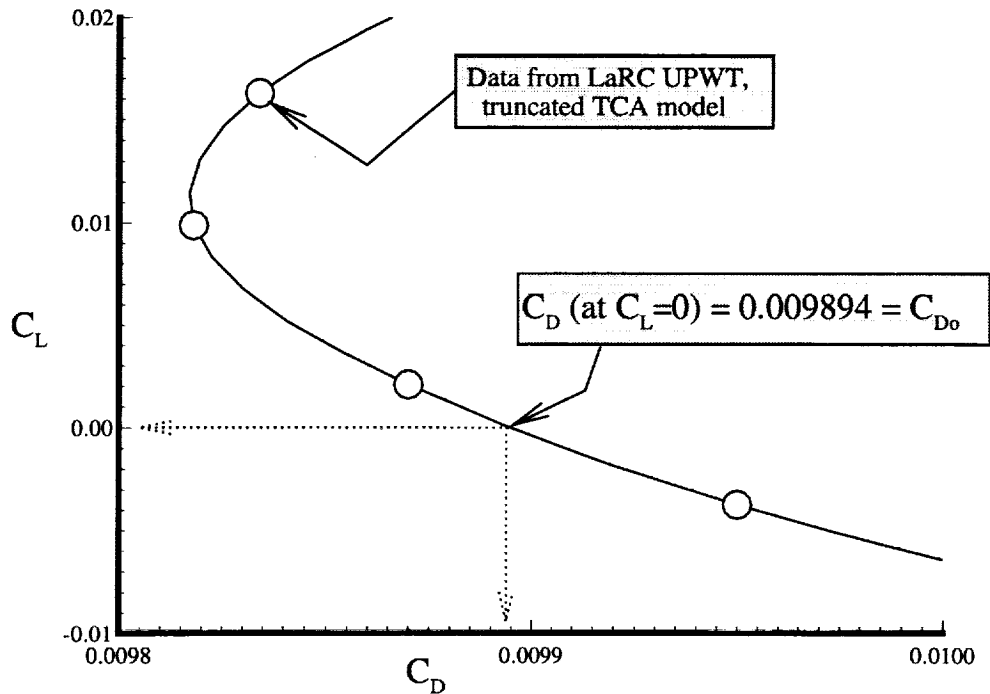


Figure 17. Experimental drag polar for the truncated TCA model. $M_\infty = 2.4$, $\beta = 0^\circ$, $R_{ft} \approx 4 \times 10^6$.

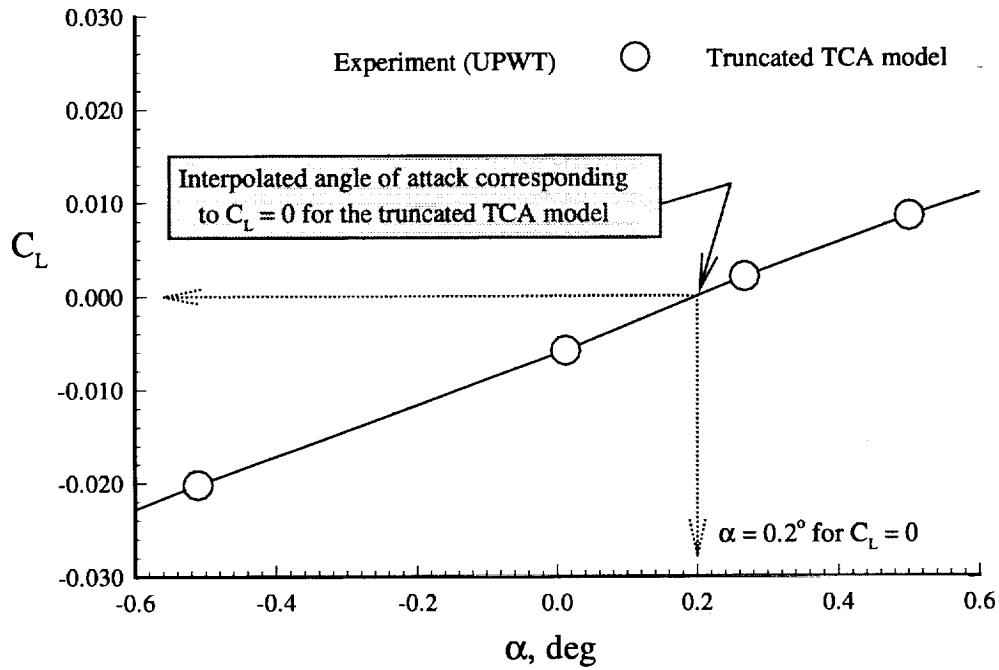


Figure 18. Experimental C_L - α curve for the truncated TCA configuration. $M_\infty = 2.4$, $\beta = 0^\circ$, $R_{ft} \approx 4 \times 10^6$.

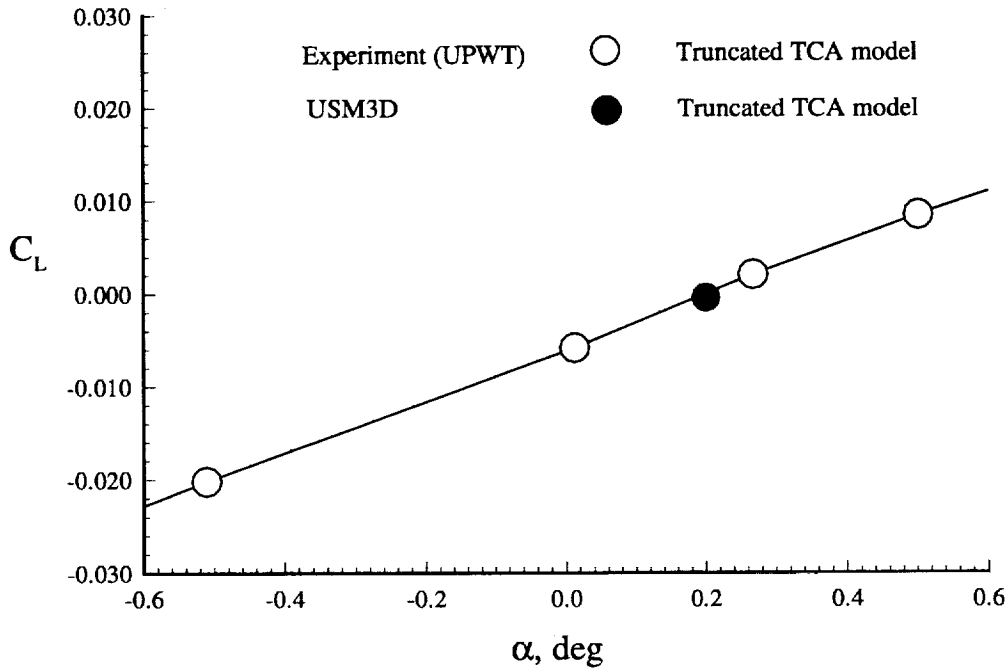


Figure 19. Computed C_L at $\alpha = 0.2$ and correlation with data. $M_\infty = 2.4$, $\beta = 0^\circ$, $R_{ft} \approx 4 \times 10^6$.

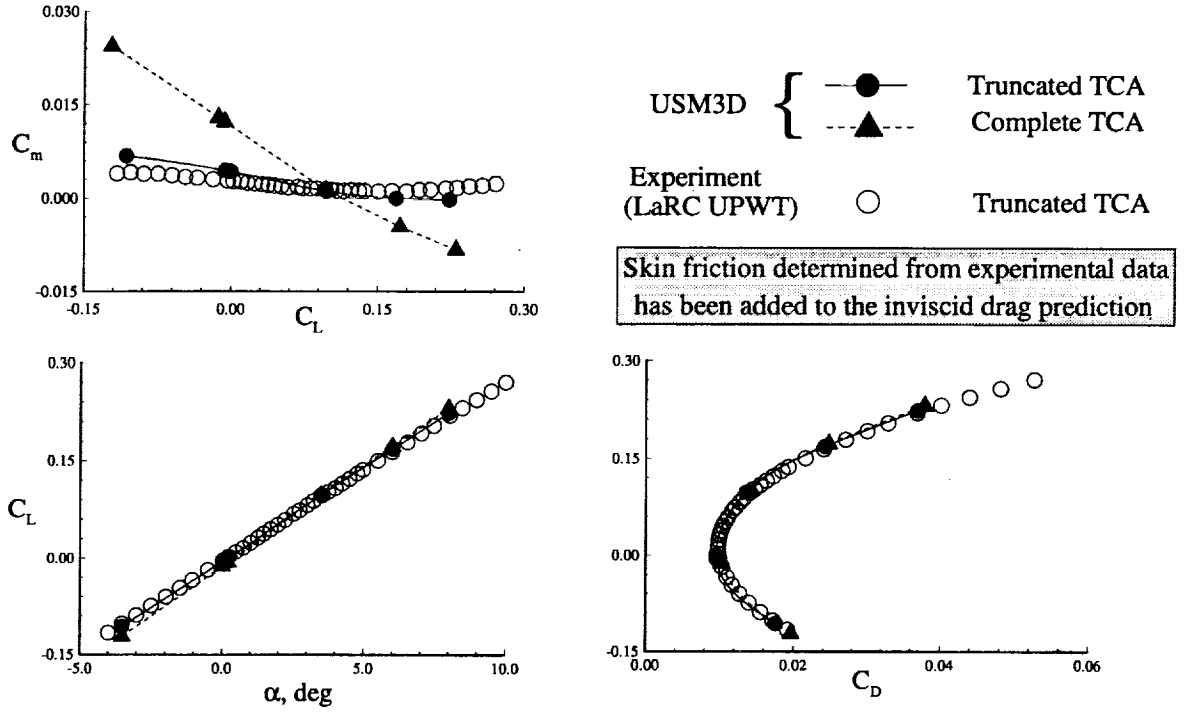


Figure 20. Computed and measured longitudinal aerodynamic characteristics. $M_\infty = 2.4$, $\beta = 0^\circ$, $R_{ft} \approx 4 \times 10^6$

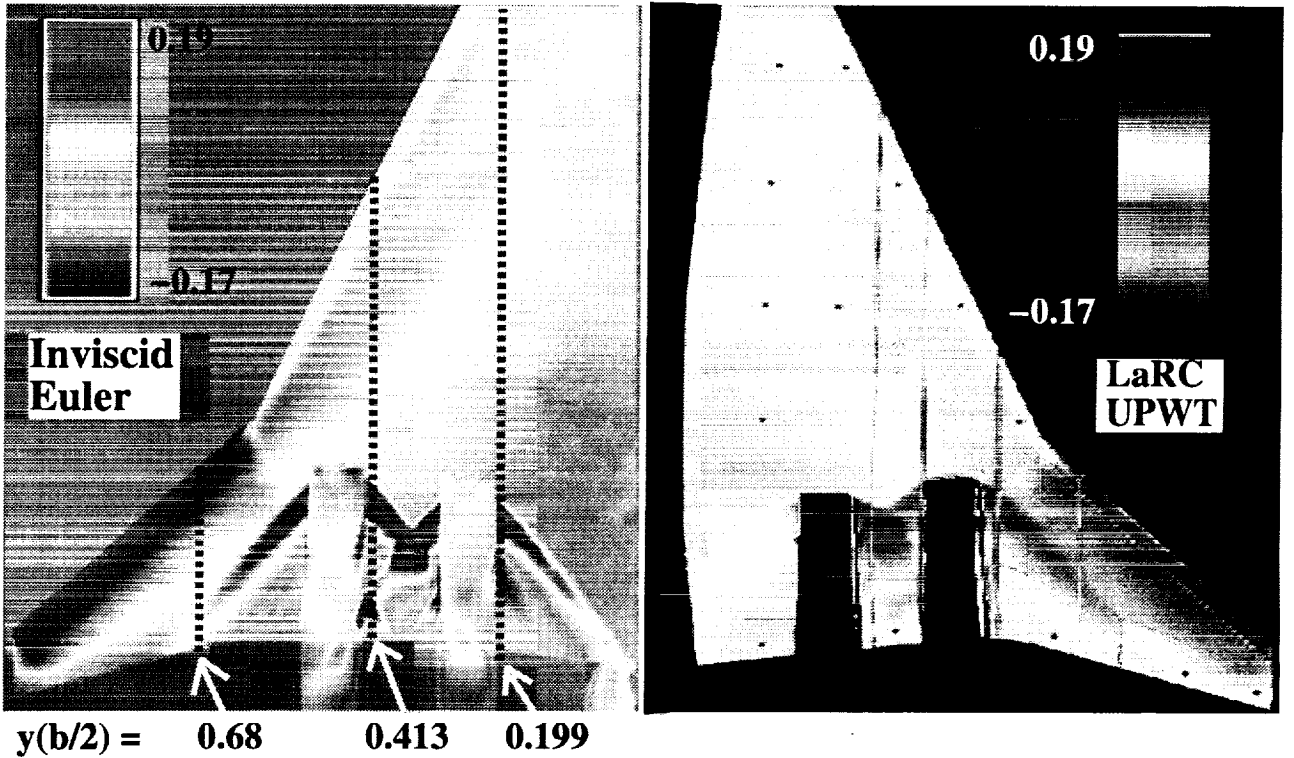


Figure 21. Computed surface C_p and correlation with PSP results. $M_\infty = 2.4$, $\alpha = 3.5^\circ$, $R_{ft} \approx 4 \times 10^6$.

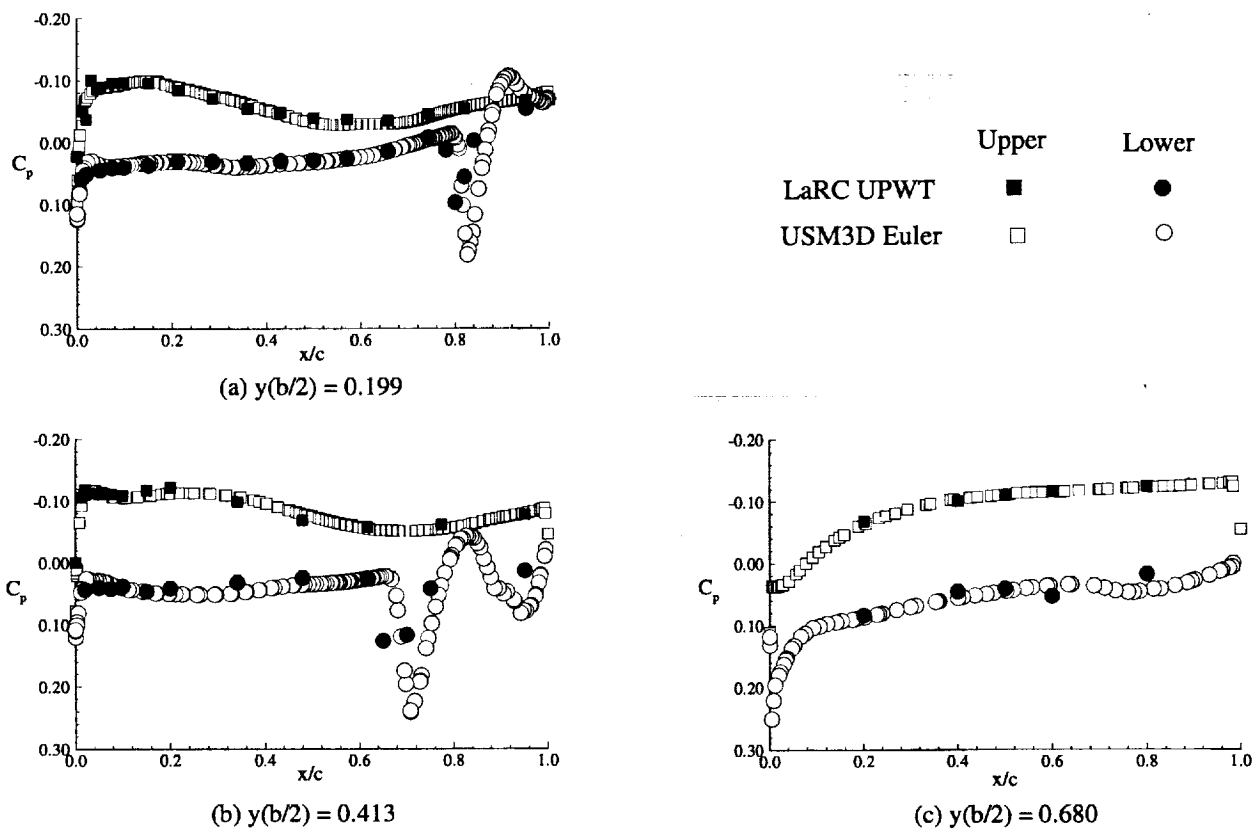


Figure 22. Computed and measured surface pressure coefficients at $M_\infty = 2.4$, $\alpha = 3.5^\circ$, $R_{ft} \approx 4 \times 10^6$.

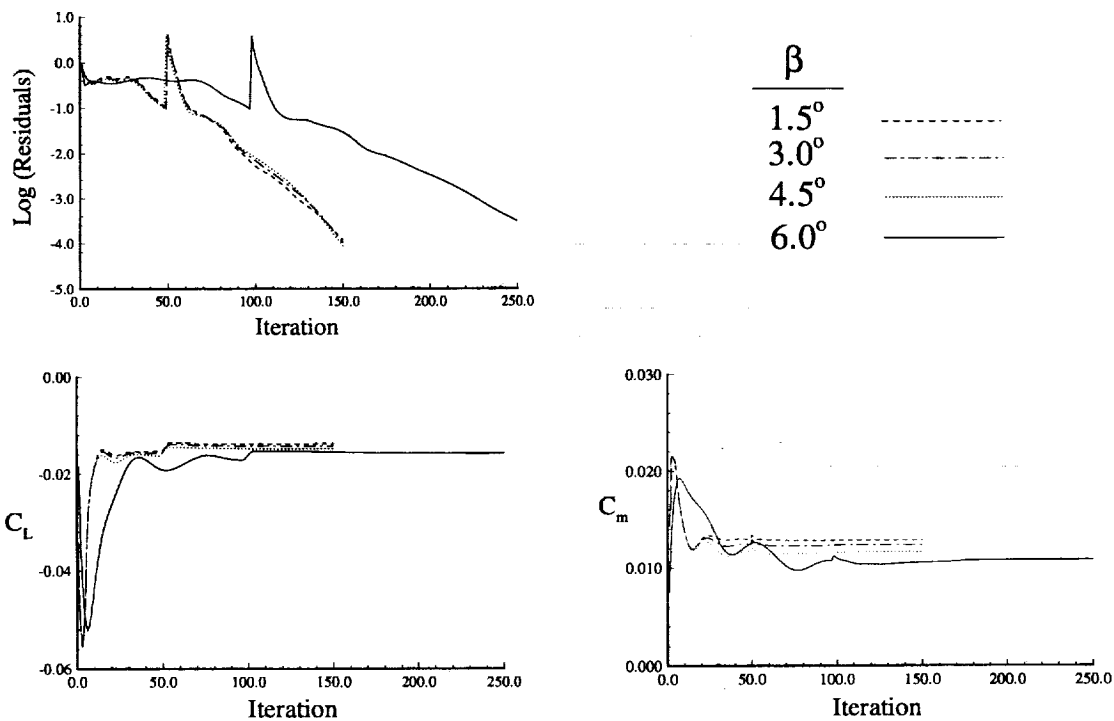
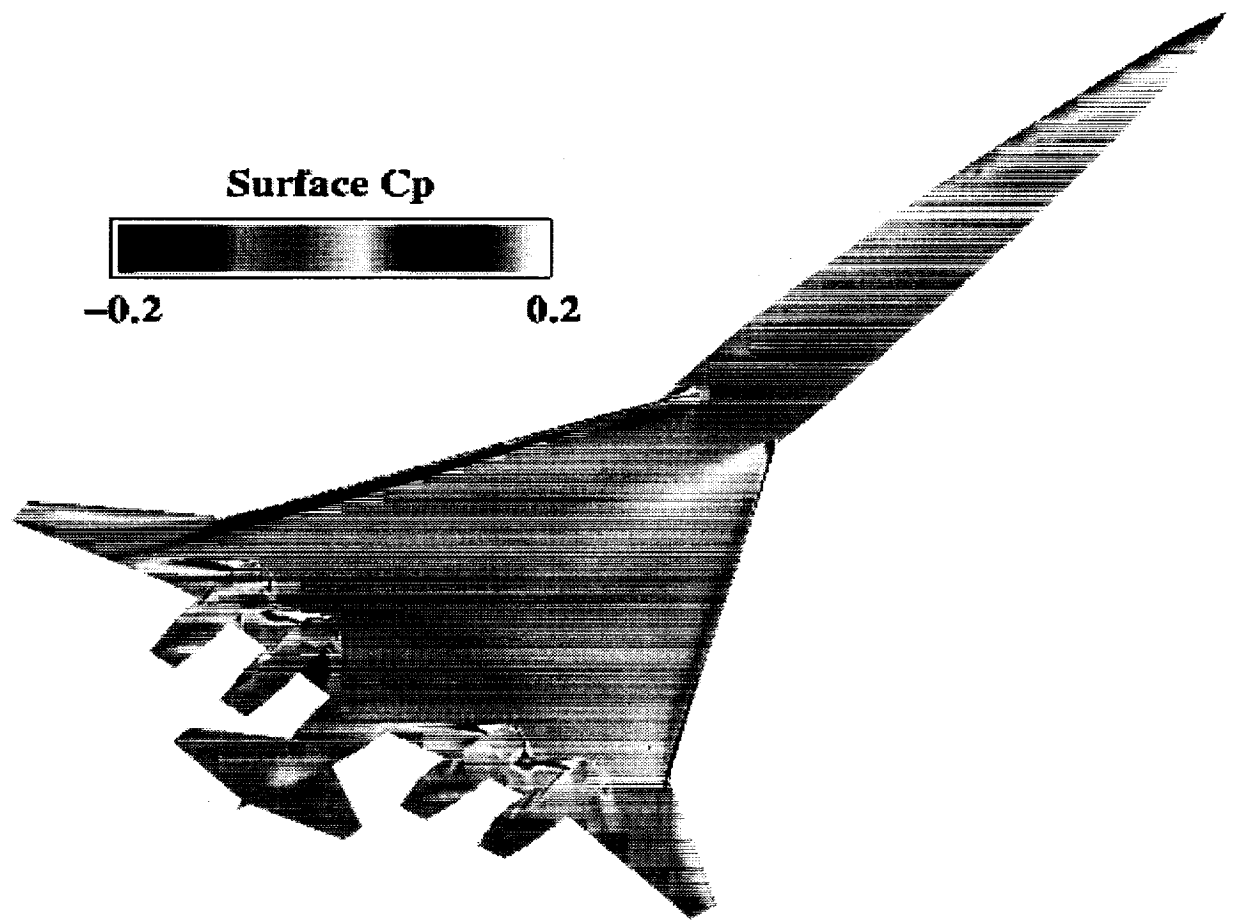
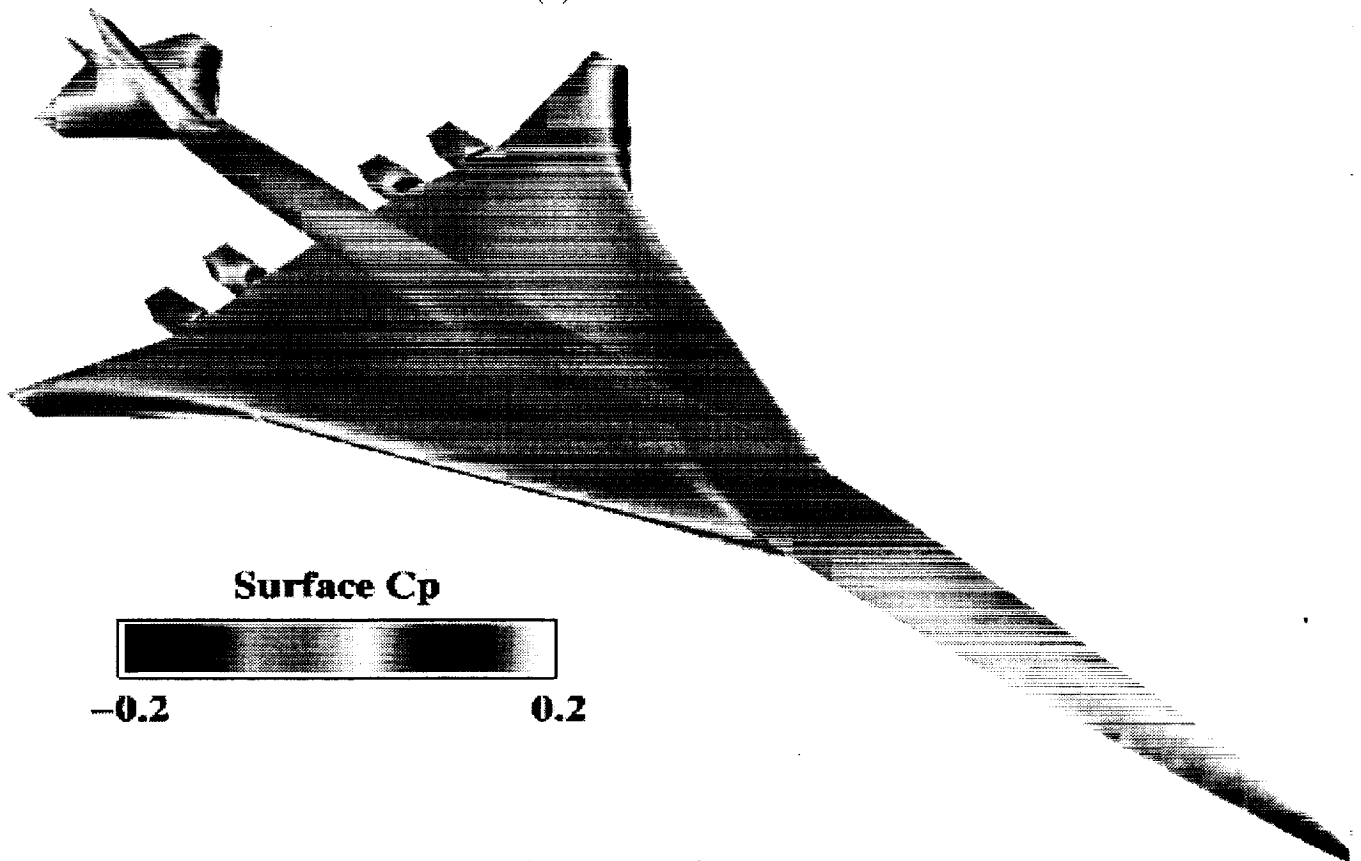


Figure 23. Solution convergence characteristics at sideslip angles. $M_\infty = 2.4$, $\alpha = 0^\circ$.



(a) Lower surface.



(b) Upper surface.

Figure 24. Computed surface C_p contours - $\alpha = 0^\circ$, $M_\infty = 2.4$, $\beta = 3^\circ$.

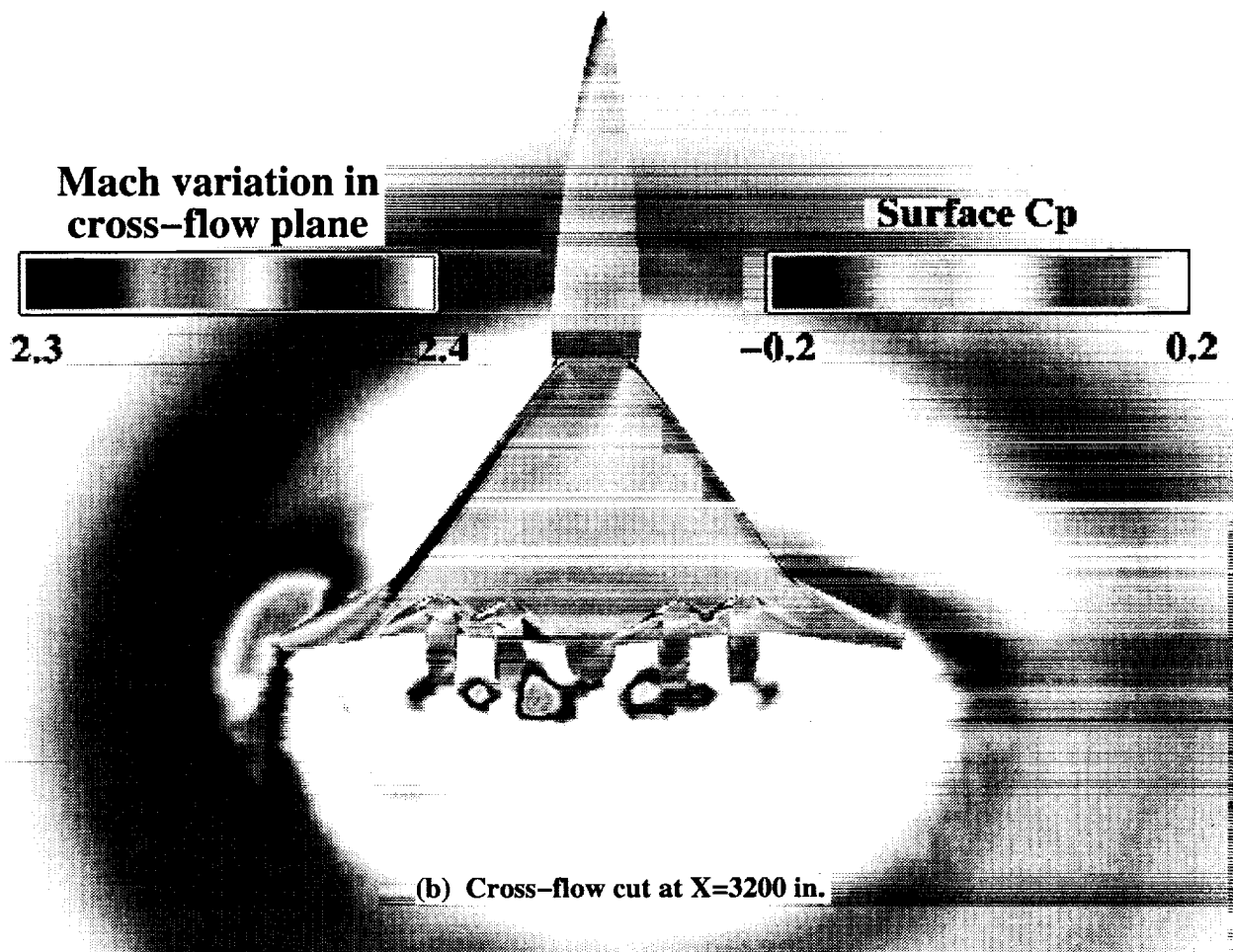
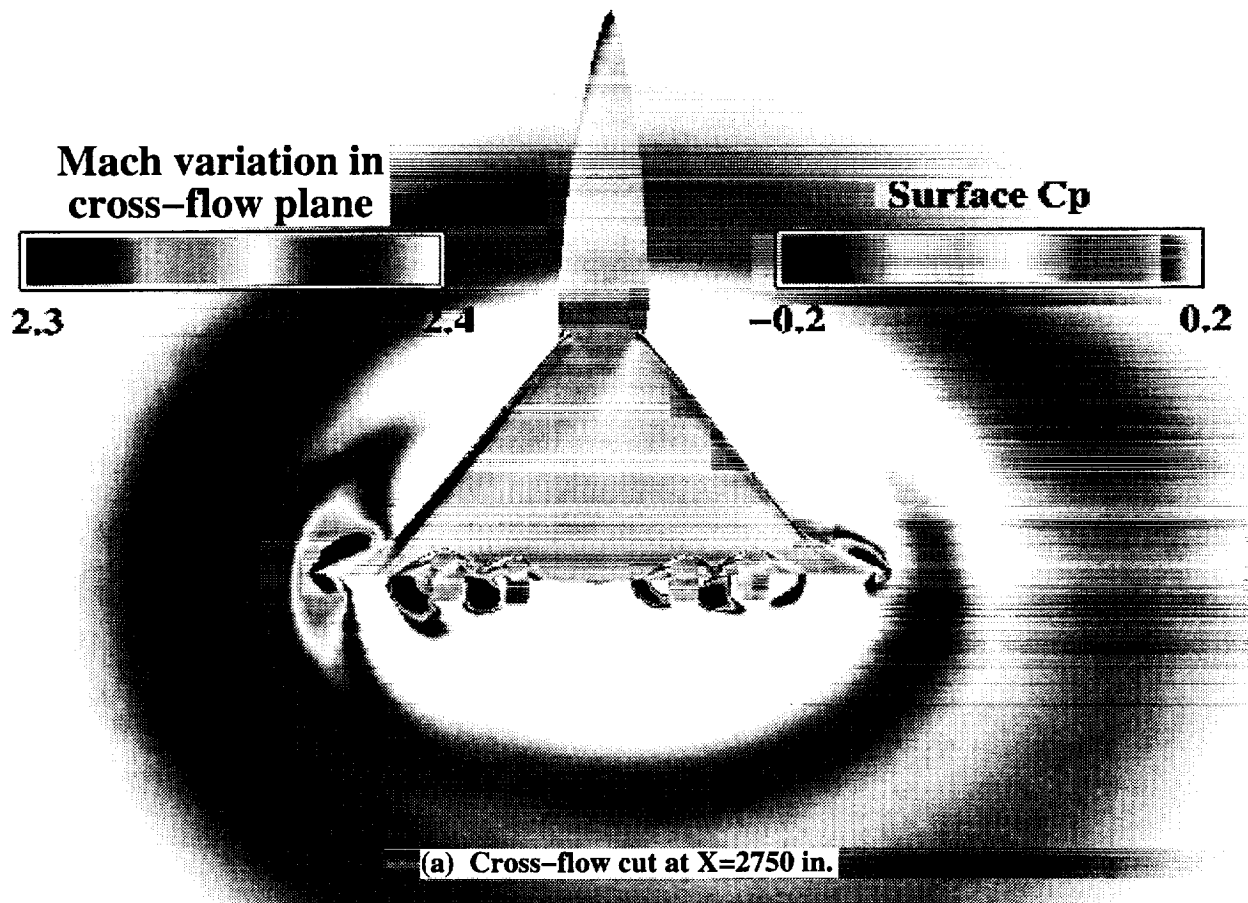


Figure 25. Computed surface C_p and Mach variation in cross-flow planes. - $\alpha = 0^\circ$, $M_\infty = 2.4$, $\beta = 3^\circ$.

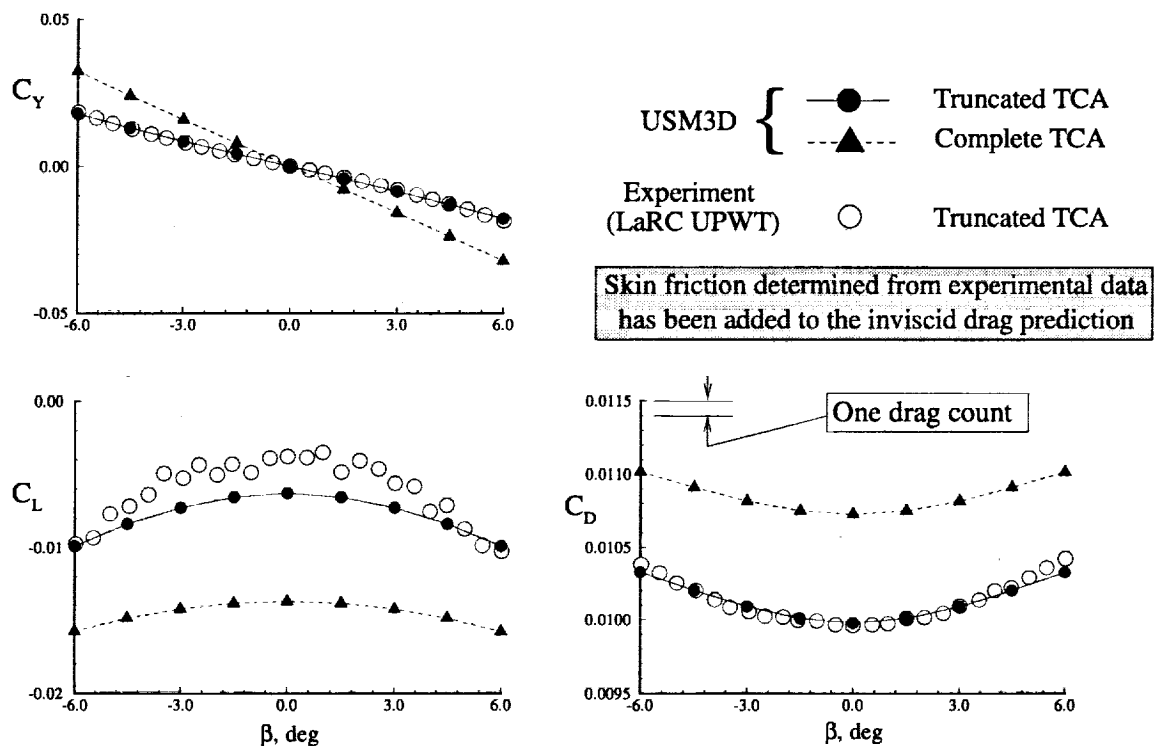


Figure 26. Computed and measured aerodynamic forces at sideslip angles. $M_\infty = 2.4$, $\alpha = 0^\circ$, $R_{ft} \approx 4 \times 10^6$

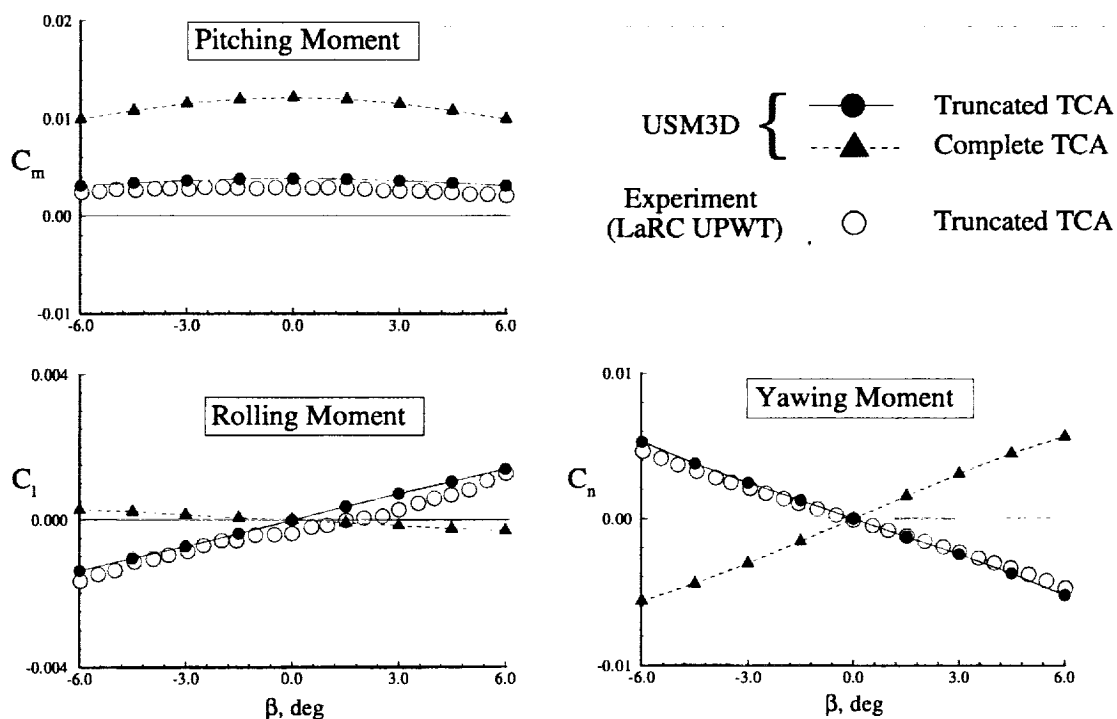


Figure 27. Computed and measured aerodynamic moments at sideslip angles. $M_\infty = 2.4$, $\alpha = 0^\circ$, $R_{ft} \approx 4 \times 10^6$

REPORT DOCUMENTATION PAGE			Form Approved OMB No. 0704-0188	
Public reporting burden for this collection of information is estimated to average 1 hour per response, including the time for reviewing instructions, searching existing data sources, gathering and maintaining the data needed, and completing and reviewing the collection of information. Send comments regarding this burden estimate or any other aspect of this collection of information, including suggestions for reducing this burden, to Washington Headquarters Services, Directorate for Information Operations and Reports, 1215 Jefferson Davis Highway, Suite 1204, Arlington, VA 22202-4302, and to the Office of Management and Budget, Paperwork Reduction Project (0704-0188), Washington, DC 20503.				
1. AGENCY USE ONLY (Leave blank)	2. REPORT DATE December 1999	3. REPORT TYPE AND DATES COVERED Technical Publication		
4. TITLE AND SUBTITLE Unstructured Grid Euler Method Assessment for Longitudinal and Lateral/Directional Aerodynamic Performance Analysis of the HSR Technology Concept Airplane at Supersonic Cruise Speed		5. FUNDING NUMBERS WU 537-07-22-24		
6. AUTHOR(S) Farhad Ghaffari				
7. PERFORMING ORGANIZATION NAME(S) AND ADDRESS(ES) NASA Langley Research Center Hampton, VA 23681-2199		8. PERFORMING ORGANIZATION REPORT NUMBER L-17737		
9. SPONSORING/MONITORING AGENCY NAME(S) AND ADDRESS(ES) National Aeronautics and Space Administration Washington, DC 20546-0001		10. SPONSORING/MONITORING AGENCY REPORT NUMBER NASA/TP-1999-209543		
11. SUPPLEMENTARY NOTES				
12a. DISTRIBUTION/AVAILABILITY STATEMENT Unclassified-Unlimited Subject Category 02 Availability: NASA CASI (301) 621-0390			12b. DISTRIBUTION CODE Distribution: Nonstandard	
13. ABSTRACT (Maximum 200 words) Unstructured grid Euler computations, performed at supersonic cruise speed, are presented for a High Speed Civil Transport (HSCT) configuration, designated as the Technology Concept Airplane (TCA) within the High Speed Research (HSR) Program. The numerical results are obtained for the complete TCA cruise configuration which includes the wing, fuselage, empennage, diverters, and flow through nacelles at $M_\infty = 2.4$ for a range of angles-of-attack and sideslip. Although all the present computations are performed for the complete TCA configuration, appropriate assumptions derived from the fundamental supersonic aerodynamic principles have been made to extract aerodynamic predictions to complement the experimental data obtained from a 1.675%-scaled truncated (aft fuselage/empennage components removed) TCA model. The validity of the computational results, derived from the latter assumptions, are thoroughly addressed and discussed in detail. The computed surface and off-surface flow characteristics are analyzed and the pressure coefficient contours on the wing lower surface are shown to correlate reasonably well with the available pressure sensitive paint results, particularly, for the complex flow structures around the nacelles. The predicted longitudinal and lateral/directional performance characteristics for the truncated TCA configuration are shown to correlate very well with the corresponding wind-tunnel data across the examined range of angles-of-attack and sideslip. The complementary computational results for the longitudinal and lateral/directional performance characteristics for the complete TCA configuration are also presented along with the aerodynamic effects due to empennage components. Results are also presented to assess the computational method performance, solution sensitivity to grid refinement, and solution convergence characteristics.				
14. SUBJECT TERMS Computational fluid dynamics; Euler formulation; Supersonic cruise; High-Speed Civil Transport; Lateral/directional; Shock waves; Unstructured grid			15. NUMBER OF PAGES 43	
			16. PRICE CODE A03	
17. SECURITY CLASSIFICATION OF REPORT Unclassified	18. SECURITY CLASSIFICATION OF THIS PAGE Unclassified	19. SECURITY CLASSIFICATION OF ABSTRACT Unclassified	20. LIMITATION OF ABSTRACT UL	